

Investigations of dust heating in M81, M83, and NGC 2403 with the Herschel Space Observatory

G. J. Bendo^{1,2}, A. Boselli³, A. Dariush^{4,5,2}, M. Pohlen⁴, H. Roussel⁶, M. Sauvage⁷, M. W. L. Smith⁴, C. D. Wilson⁸, M. Baes⁹, A. Cooray¹⁰, D. L. Clements², L. Cortese¹¹, K. Foyle⁸, M. Galametz¹², H. L. Gomez⁴, V. Lebouteiller⁷, N. Lu^{13,14}, S. C. Madden⁷, E. Mentuch⁸, B. O’Halloran², M. J. Page¹⁵, A. Remy⁷, B. Schulz¹⁶, L. Spinoglio¹⁷

¹ UK ALMA Regional Centre Node, Jodrell Bank Centre for Astrophysics, School of Physics and Astronomy, University of Manchester, Oxford Road, Manchester M13 9PL, United Kingdom

² Astrophysics Group, Imperial College, Blackett Laboratory, Prince Consort Road, London SW7 2AZ, United Kingdom

³ Laboratoire d’Astrophysique de Marseille, UMR6110 CNRS, 38 rue F. Joliot-Curie, F-13388 Marseille, France

⁴ School of Physics and Astronomy, Cardiff University, Queens Buildings, The Parade, Cardiff CF24 3AA, United Kingdom

⁵ School of Astronomy, Institute for Research in Fundamental Sciences (IPM), PO Box 19395-5746, Tehran, Iran

⁶ Institut d’Astrophysique de Paris, UMR7095 CNRS, Université Pierre & Marie Curie, 98 bis Boulevard Arago, 75014 Paris, France

⁷ Laboratoire AIM, CEA, Université Paris Diderot, IRFU/Service d’Astrophysique, Bat. 709, 91191 Gif-sur-Yvette, France

⁸ Department of Physics & Astronomy, McMaster University, Hamilton, Ontario L8S 4M1, Canada

⁹ Sterrenkundig Observatorium, Universiteit Gent, Krijgslaan 281 S9, B-9000 Gent, Belgium

¹⁰ Department of Physics and Astronomy, University of California, Irvine, CA 92697, USA

¹¹ European Southern Observatory, Karl-Schwarzschild Str. 2, 85748 Garching bei Muenchen, Germany

¹² Institute of Astronomy, University of Cambridge, Madingley Road, Cambridge CB3 0HA, United Kingdom

¹³ Jet Propulsion Laboratory, Pasadena, CA 91109, USA

¹⁴ Department of Astronomy, California Institute of Technology, Pasadena, CA 91125, USA

¹⁵ Mullard Space Science Laboratory, University College London, Holmbury St Mary, Dorking, Surrey RH5 6NT, United Kingdom

¹⁶ Infrared Processing and Analysis Center, California Institute of Technology, Mail Code 100-22, 770 South Wilson Av, Pasadena, CA 91125, USA

¹⁷ Istituto di Fisica dello Spazio Interplanetario, INAF, Via del Fosso del Cavaliere 100, I-00133 Roma, Italy

ABSTRACT

We use *Spitzer* Space Telescope and *Herschel* Space Observatory far-infrared data along with ground-based optical and near-infrared data to understand how dust heating in the nearby face-on spiral galaxies M81, M83, and NGC 2403 is affected by the starlight from all stars and by the radiation from star forming regions. We find that 70/160 μm surface brightness ratios tend to be more strongly influenced by star forming regions. However, the 250/350 μm and 350/500 μm surface brightness ratios are more strongly affected by the light from the total stellar populations, suggesting that the dust emission at $>250 \mu\text{m}$ originates predominantly from a component that is colder than the dust seen at $<160 \mu\text{m}$ and that is relatively unaffected by star formation activity. We conclude by discussing the implications of this for modelling the spectral energy distributions of both nearby and more distant galaxies and for using far-infrared dust emission to trace star formation.

Key words: galaxies: ISM, galaxies: spiral, infrared: galaxies, galaxies: individual: M81, galaxies: individual: M83, galaxies: individual: NGC 2403,

1 INTRODUCTION

Since the launch of the Infrared Astronomical Satellite (IRAS; Neugebauer et al. 1984), astronomers have frequently used far-infrared emission to trace star formation in extragalactic sources. Far-infrared emission has been very popular to use for estimating star formation rates because it is not as strongly affected by dust extinction as ultraviolet and optical tracers of star formation and because many surveys, particularly surveys of high-redshift sources, have detected a multitude of galaxies in

the far-infrared. Several equations have been derived to calculate star formation rates either from far-infrared measurements by themselves or from far-infrared data combined with optical or ultraviolet data (Scoville & Young 1983; Buat & Xu 1996; Kennicutt 1998a; Kennicutt et al. 2009). While it is commonly assumed in the use of these equations that dust is primarily if not solely heated by star forming regions, the heating source for the dust producing far-infrared emission has been widely debated for decades. Following the completion of the IRAS surveys, several papers showed that IRAS 60 and 100 μm emission was strongly

correlated with star formation activity (e.g. Devereux & Young 1990; Devereux et al. 1995; Buat & Xu 1996), while others argued that a significant fraction of dust emission originated from dust heated by evolved stars (e.g. Lonsdale Persson & Helou 1987; Walterbos & Schwering 1987; Sauvage & Thuan 1992; Walterbos & Greenawalt 1996; Kong et al. 2004). Additionally, analyses performed by Devereux & Young (1992) and Devereux & Young (1993) on IRAS data combined with 160 or 170 μm data from the Kuiper Airborne Observatory indicated that emission at $>100 \mu\text{m}$ also originated from dust heated by star formation. Later observations of nearby spiral galaxies with the *Spitzer* Space Telescope (Werner et al. 2004) demonstrated that optical and ultraviolet star formation tracers were very strongly correlated with 24 μm dust emission (Calzetti et al. 2005, 2007; Prescott et al. 2007; Kennicutt et al. 2007, 2009; Zhu et al. 2008) or with total infrared emission (Kennicutt et al. 2009). However, similar analyses showed that the correlation between optical/ultraviolet star formation tracers and either 70 or 160 μm emission was weaker (Calzetti et al. 2010), which implied that not all of the far-infrared emission originated from dust heated by star formation. Additionally, Hinz et al. (2004) demonstrated that large scale 160 μm emission from M33 qualitatively appeared more similar to large scale K-band emission than to large scale $\text{H}\alpha$, 24 μm , or 70 μm emission, implying that the dust emitting at 160 μm was at least partly heated by the evolved stellar population. Furthermore, some dust models applied to IRAS, Infrared Space Observatory (Kessler et al. 1996), *Spitzer*, and ground-based submillimetre data for nearby galaxies have suggested that heating by evolved stars was needed to reproduce the observed spectral energy distributions for these galaxies (e.g. Draine et al. 2007; da Cunha et al. 2008; Bianchi 2008; Popsecu et al. 2011).

The first results from the *Herschel* Space Observatory (Pilbratt et al. 2010) brought attention back to this issue mainly because the telescope provided data at longer wavelengths than what had been provided by either IRAS or *Spitzer* and at a higher signal-to-noise than what was possible with ground-based instrumentation. Bendo et al. (2010b) demonstrated that colours between 160 and 500 μm in M81, an Sab galaxy (de Vaucouleurs et al. 1991), were more strongly dependent on galactocentric radius than on far-infrared surface brightness, which implies that the dust was heated primarily by the evolved stars in the galaxy (which have a surface brightness that varies primarily with radius) rather than by star forming regions (which are primarily found in the infrared-bright regions). In contrast, Boquien et al. (2010) and Verlet et al. (2010) found that 100-250 μm emission from compact sources in M33, an Scd galaxy (de Vaucouleurs et al. 1991), were strongly correlated with star formation as measured using $\text{H}\alpha$ emission, 24 μm emission, or a combination of the two.

The goal of this paper is to follow-up these early *Herschel* results using three nearby face-on spiral galaxies with differing Hubble types taken from the Very Nearby Galaxies Survey, a *Herschel* guaranteed-time photometric and spectroscopic survey of 13 galaxies with the Photodetector Array Camera and Spectrometer (PACS; Poglitsch et al. 2010) and Spectral and Photometric Imaging Receiver (SPIRE; Griffin et al. 2010). We will primarily compare surface brightness ratios between two *Herschel* bands to both stellar surface brightness and to star formation rate. Surface brightnesses measured in single bands may be correlated to star formation through dust heating, in which the dust is heated by the star forming regions and becomes more luminous, or through the Schmidt law (Schmidt 1959; Kennicutt 1998b), in which star formation is correlated to the amount of dust present. In contrast, surface brightness

ratios are advantageous to use in that they are largely independent of the total dust surface density. Instead, surface brightness ratios will primarily depend only on the average temperature of the dust emitting at those wavelengths, with temperature variations caused either by variations in the amount of a warmer dust component relative to a colder dust component or variations in the overall temperature of a single dust component. This is similar to the approach used by Bendo et al. (2010b), but the advantage of the analysis in this paper is that we will not rely upon galactocentric radius as a proxy for the surface brightness of the evolved stellar population and that we will use a better tracer of star formation.

Section 2 describes the three galaxies in our sample (M81, M83, and NGC 2403) and why they are well-suited for this analysis. Section 3 provides an overview of the data from *Herschel* and from other sources as well as details on the preparation of the data for the analysis. The analysis itself is presented in Section 4, the implications of the results is discussed in Section 5, and a summary is provided in Section 6.

2 SAMPLE GALAXIES

As stated above, the three galaxies used for this analysis were all galaxies selected from the Very Nearby Galaxies Survey (PI: C. Wilson), a guaranteed-time survey of 13 well-studied nearby galaxies with a diverse range of properties. The galaxies for the analysis in this paper were selected because they are all spiral galaxies with inclinations of $\lesssim 60^\circ$ from face-on, they have optical discs larger than 10 arcmin, and they are at distances of less than 5 Mpc, so sub-kpc structures can be easily studied within the galaxies. The galaxies are also roughly representative of early-, mid-, and late type spiral galaxies. Details on the three galaxies used in this analysis are given in Table 1. The images used in the analysis are shown in Figures 1-3.

M81 (NGC 3031) is an Sab galaxy (de Vaucouleurs et al. 1991) that is the brightest galaxy in the M81 Group (Karachentsev et al. 2002). As this is an early-type spiral galaxy, the bulge is a relatively large and bright component of the galaxy. The dust emission is unusually extended compared to other early-type spiral galaxies; the dust distribution is similar to late-type spiral galaxies (Bendo et al. 2007). The dust emission also does not qualitatively appear similar to the stellar emission. Furthermore, the star forming regions lie primarily in the outer disc, whereas the centre of the galaxy is relatively devoid of star formation, as shown by the $\text{H}\alpha$ image (also see Devereux et al. 1995; Allen et al. 1997), although incompletely-subtracted continuum emission from the bulge is visible in the image. Consequently, this galaxy is very useful for differentiating between effects related to heating by starlight and effects related to heating by star forming regions. The galaxy does contain a low luminosity active galactic nucleus (AGN; Markoff et al. 2008; Moustakas et al. 2010) that could affect the observed spectral energy distribution (SED) for the nuclear region. We comment on this in the analysis where appropriate. Also, the 250-500 μm images show that the galaxy is surrounded by extended emission that was determined to be foreground cirrus emission by (Davies et al. 2010). The foreground structures are fainter than much of the emission from M81 itself, so by choosing appropriate surface brightness thresholds for our analysis, we avoid working with data that is strongly affected by the foreground emission.

M83 (NGC 5236) is an Sc galaxy (de Vaucouleurs et al. 1991) with a grand design appearance (Elmegreen & Elmegreen 1987).

Table 1. Basic data on sample galaxies.

Galaxy	Hubble Type ^a	Size of Optical Disc (arcmin) ^b	Position Angle of Major Axis ^{b,c}	Inclination	Distance (Mpc)	Physical Size of 36 arcsec (pc) ^d
M81 (NGC 3031)	SA(s)ab	26.9×14.1	157°	59.0° ^e	3.6 ± 0.4 ^f	630 ± 70
M83 (NGC 5236)	SAB(s)c	12.1×11.5	45° ^g	24° ^g	4.5 ± 0.2 ^h	790 ± 30
NGC 2403	SAB(s)cd	21.9×12.3	127°	62.9° ^e	3.2 ± 0.3 ^f	560 ± 50

^a Hubble types are from de Vaucouleurs et al. (1991).

^b Data are for the D_{25} isophote as given by de Vaucouleurs et al. (1991) except where specified.

^c Position angle is defined as degrees from north through east.

^d This angular size represents the size of the bins used in the analysis in this paper. See Section 3.4 for information on the selection of this bin size.

^e Data are taken from de Bok et al. (2008).

^f Data are taken from Freedman et al. (2001).

^g Data are taken from Comte (1981).

^h Data are taken from Thim et al. (2003).

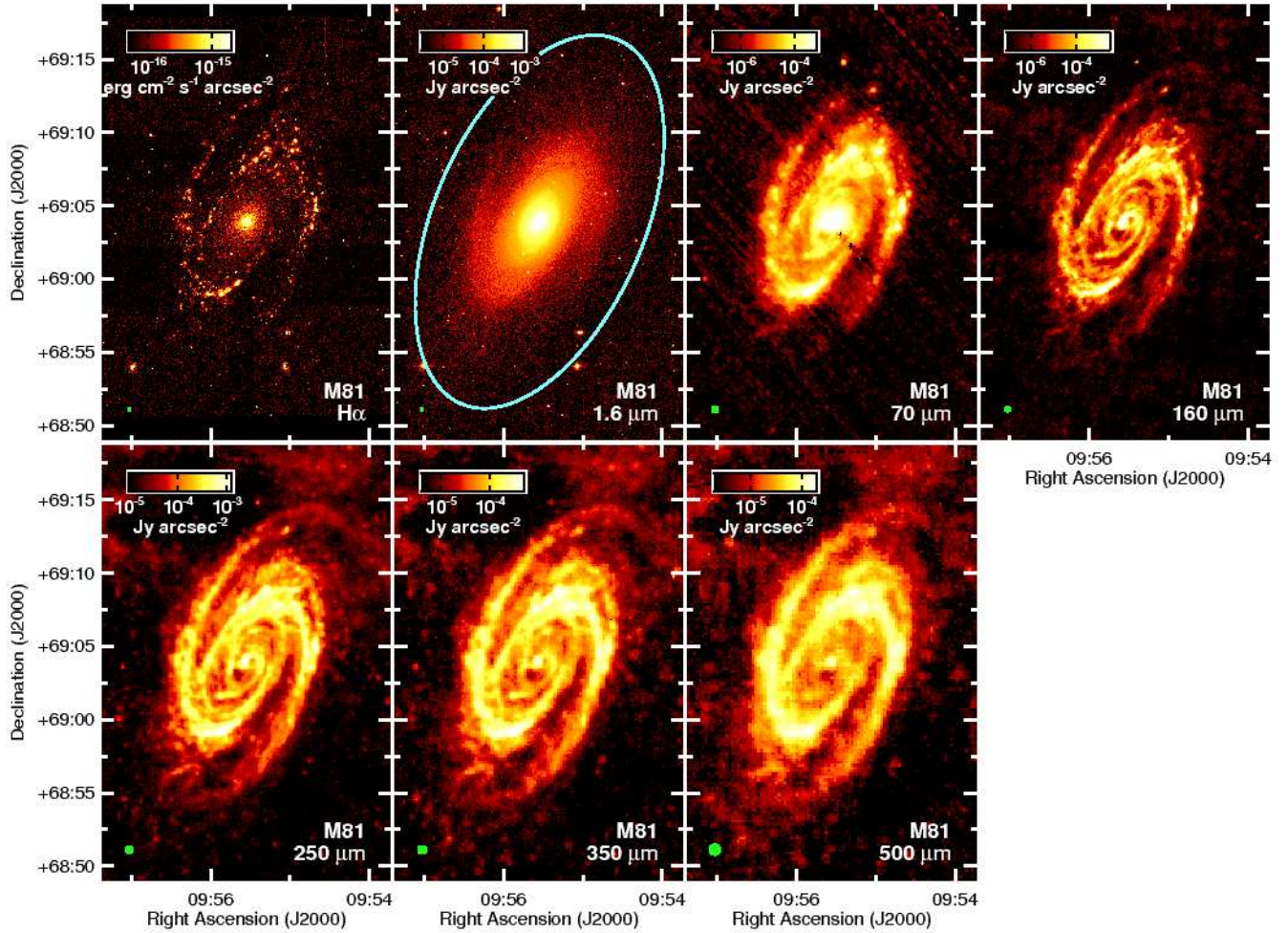


Figure 1. The 30×20 arcmin images of M81 used in this analysis. The $H\alpha$ emission traces the gas that is photoionised by star forming regions (although, in the case of M81, some residual continuum emission from the bulge is present). The $1.6 \mu\text{m}$ image traces the total stellar population. The $70\text{--}500 \mu\text{m}$ emission trace the thermal emission from colder dust within the galaxy. North is up and east is left in each panel. The green circles in the lower left corner of each panel shows the FWHM of the data. The cyan ellipse in the $1.6 \mu\text{m}$ image shows the optical disk of the galaxy.

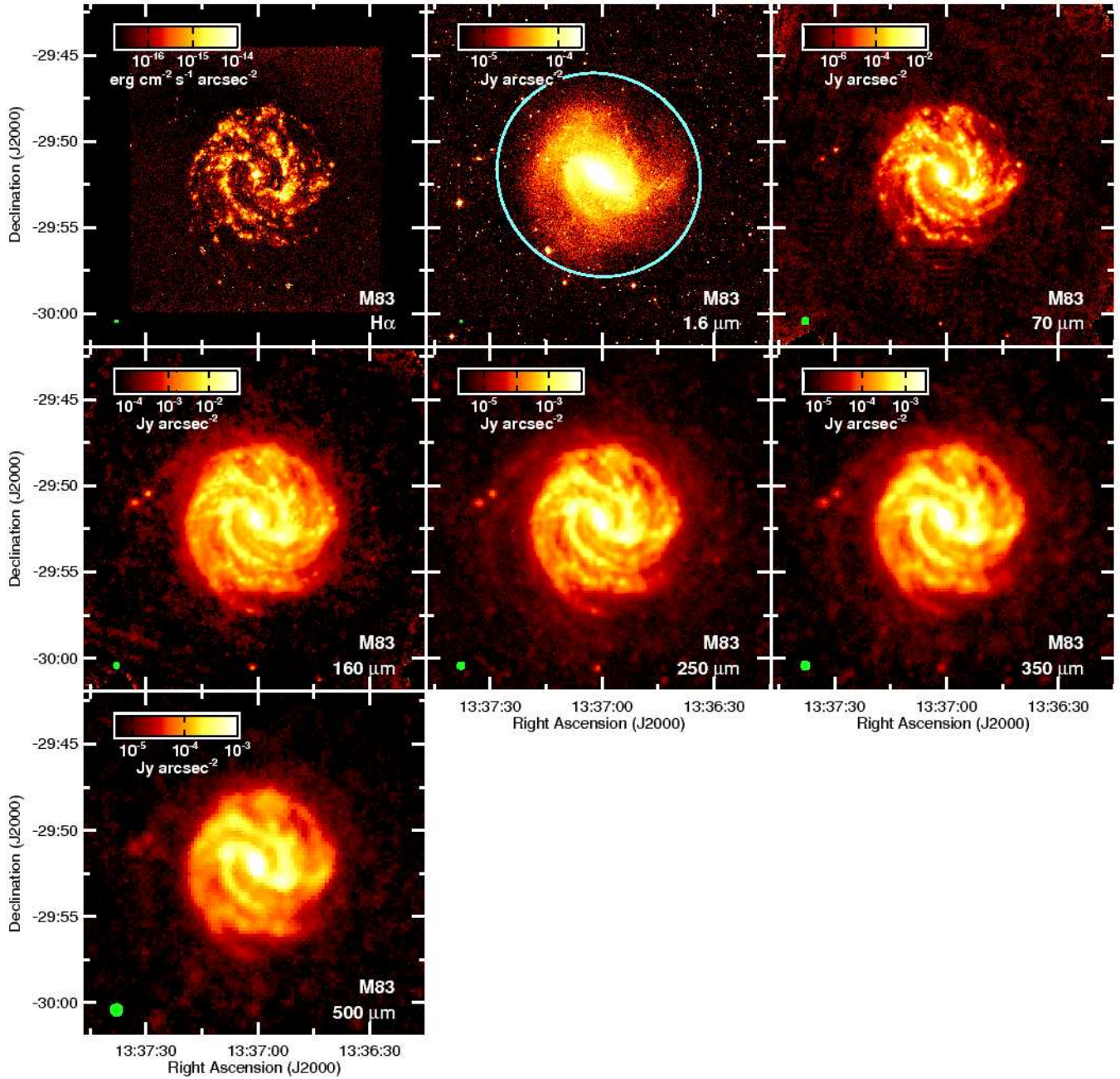


Figure 2. The 20×20 arcmin images of M83 used in this analysis. See the caption of Figure 1 for other information.

While the centre is the site of a strong starburst (e.g. Talbot et al. 1979; Telesco & Harper 1980; Condon et al. 1982; Bohlin et al. 1983; Trinchieri et al. 1985; Turner et al. 1987), star formation rates in the disc are not as extreme. Unlike the other two galaxies in this analysis, M83 is a case where the stellar emission and dust emission look qualitatively similar. However, it should be representative of many other nearby grand-design Sb-Sc galaxies.

NGC 2403 is an Scd galaxy (de Vaucouleurs et al. 1991) with a flocculent appearance (Elmegreen & Elmegreen 1982, 1987). The galaxy is the second brightest galaxy in the M81 Group (Karachentsev et al. 2002). The extended, asymmetric dust emission in this galaxy is typical of many Sc-Sd galaxies (Bendo et al. 2007). The distribution of star forming regions in NGC 2403 differs

significantly from the distribution of starlight; while the starlight peaks in the centre of the galaxy, the regions with the strongest star forming activity are actually seen off-centre, as seen in H-alpha shown here as well as H-alpha and 24 micrometers images shown in previous publications (e.g. Drissen et al. 1999; Bendo et al. 2008). The star forming region with the highest H-alpha and 24 micrometers emission, which is labeled as region 44 (VS 44) in the catalogue of Véron & Sauvayre (1965) and region 128 in the catalogue by Hodge & Kennicutt (1983), is located northeast of the centre of the galaxy. Since this galaxy has multiple bright, off-centre star forming regions, it is extremely useful for disentangling effects dependent on star formation from effects dependent on either radius or starlight.

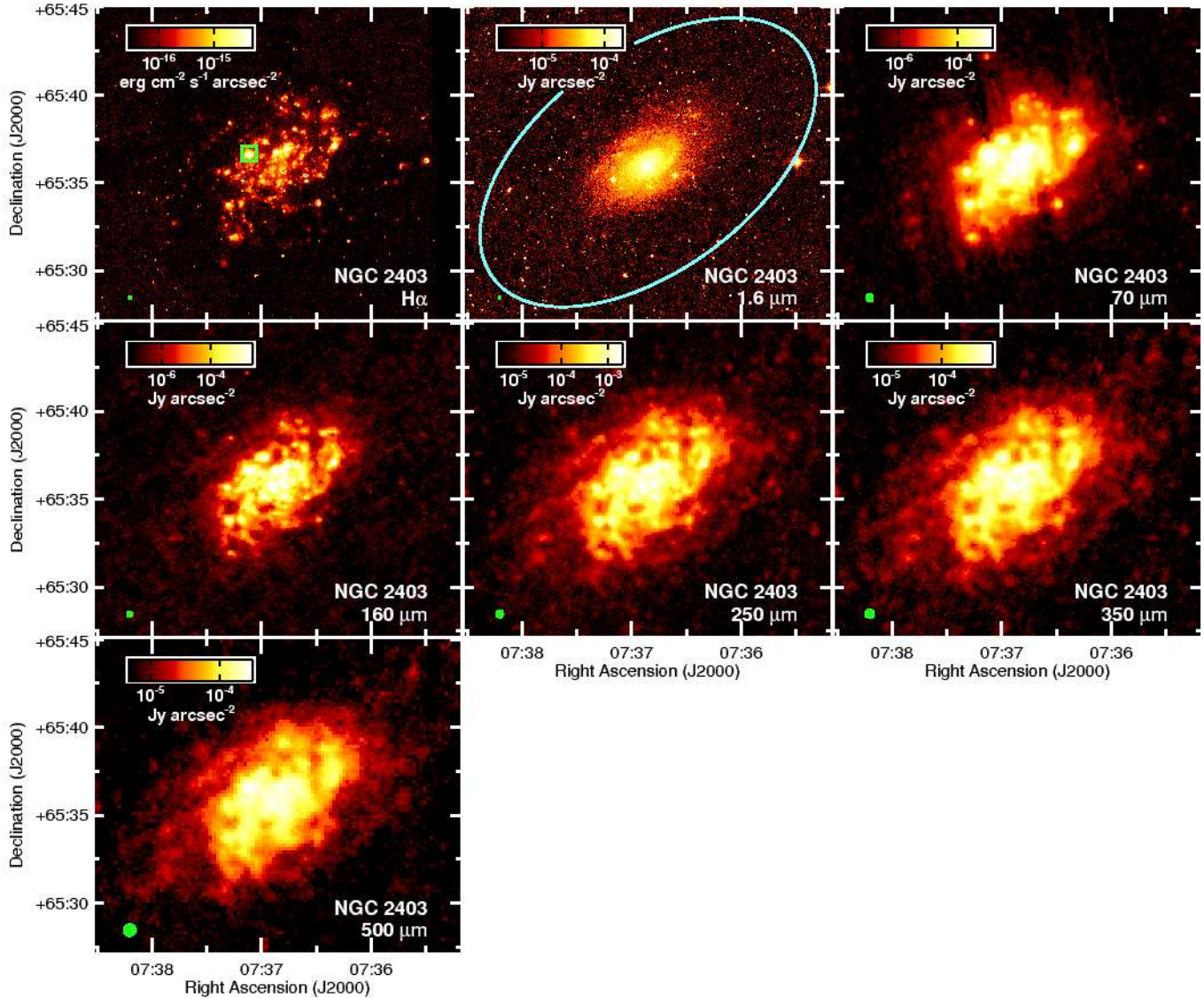


Figure 3. The 21×18 arcmin images of NGC 2403 used in this analysis. The star forming region with the highest $H\alpha$ intensity (VS 44) is marked with a green square. See the caption of Figure 1 for additional information.

3 OBSERVATIONS AND DATA REDUCTION

3.1 Far-infrared and submillimetre data

3.1.1 MIPS 70 μ m data

Although 70 μ m images were produced at the same time as 160 μ m images with PACS, we decided to use MIPS 70 μ m data for M81 and NGC 2403. PACS data have a smaller point spread function (PSF) than the MIPS data, so PACS data can be used to map structures on finer scales. As we will be matching the PSFs of the 70 μ m images to the wider PSF of the SPIRE 500 μ m images, the PSF size is not important for our analysis. Comparisons between the PACS and MIPS 70 μ m data for our sample showed that the MIPS data are more sensitive to extended emission, which is more important for our analysis (although both the PACS and MIPS 160 μ m images have similar sensitivities). However, the MIPS 70 μ m data suffer from latent image effects from bright sources that manifest themselves as dark streaks in the MIPS data. Hence, the PACS data

are preferable to use for brighter sources, while the MIPS data are preferable to use for fainter sources. In the M81 and NGC 2403 data, the latent image effects are less problematic than the lower sensitivity of the PACS data, which is why we decided to use the MIPS data for the analysis on those galaxies. In images of M83, however, the PACS data have a sufficiently high signal-to-noise that the sensitivity issues are not as much of a concern, and the MIPS images are strongly affected by latent image effects, so we use PACS 70 μ m data for that galaxy.

The 70 μ m images for M81 and NGC 2403 were acquired with the Multiband Imaging Photometer for *Spitzer* (MIPS; Rieke et al. 2004) as part of the *Spitzer* Infrared Nearby Galaxies Survey (SINGS; Kennicutt et al. 2003). These observations consist of two scan map observations performed using the medium scan rate ($6.5 \text{ arcsec s}^{-1}$). The raw data from the *Spitzer* archive were reprocessed using the MIPS Data Analysis Tools (Gordon et al. 2005) along with additional processing steps. First, ramps were fit to the

reads to derive slopes. In this step, readout jumps and cosmic ray hits were also removed, and an electronic nonlinearity correction was applied. Next, the stim flash frames (frames of data in which a calibration light source was flashed at the detectors) were used as responsivity corrections. After this, the dark current was subtracted from the data, and an illumination correction was applied. Following this, short term variations in the signal (often referred to as drift) were removed, and additional periodic variations in the background related to the stim flash cycle were subtracted; this also subtracted the background from the data. Next, a robust statistical analysis was applied to cospatial pixels from different frames in which statistical outliers (which could be pixels affected by cosmic rays) were masked out. Once this was done, final mosaics were made using pixel sizes of 4.5 arcsec. The residual backgrounds in the data were measured in regions outside the optical discs of the galaxies and subtracted, and then flux calibration factors (given as 702 MJy sr^{-1} [MIPS instrumental unit] $^{-1}$ by Gordon et al. (2007)) were applied to the data. An additional nonlinearity correction given as

$$I_{70\mu\text{m}}(\text{true}) = 0.581(I_{70\mu\text{m}}(\text{measured}))^{1.13} \quad (1)$$

by Dale et al. (2005) was applied where the surface brightness exceeded 66 MJy sr^{-1} . We also applied a colour correction of 0.901 for a 30 K blackbody given by Stansberry et al. (2007); the actual dust temperatures may differ from this value, but we anticipate that the associated colour correction will be within 10% of this value. The final data have a point spread function (PSF) with a full-width half-maximum (FWHM) of 18 arcsec according to Gordon et al. (2007). Calibration and nonlinearity uncertainties are estimated to be 10% (Gordon et al. 2007).

3.1.2 PACS 70-160 μm data

The PACS observations were performed as pairs of orthogonal scans using a 20 arcsec s^{-1} scan rate. PACS can perform simultaneous observations in only two wave bands; the VNGS chose the 70 and $160 \mu\text{m}$ bands since they were expected to bracket the peak of the SED better. Four pairs of observations were performed on each galaxy. The observations covered areas of 40×40 arcmin around M81 and NGC 2403 and 25×25 arcmin around M83 so as to sample an area with a size that is at least 1.5 times the optical disc.

The PACS data were reduced with the *Herschel* Interactive Processing Environment (HIPE) version 5.0 (Ott 2010) and a pipeline adapted from the official one. After applying the standard tasks that reformat the telemetry, associate them with the correct pointing information, and flat-field and calibrate the signal into Jy pixel^{-1} , we have applied the following specific treatments. First we deal with the possibility for electrical crosstalk, which potentially affects column 0 of all matrices (groups of 16×16 bolometers in the PACS arrays) when a bright source illuminates column 15, by systematically masking columns 0. Then we proceed to scan the signal for glitches (cosmic rays) and other possible outliers. We use the so-called second-level method, where what we scan are not the individual pixel timelines but rather reconstructed timelines made of all samples acquired on a given position of the sky. We use the `timeordered` option that is more robust to the presence of strong brightness gradients in the sky. We check that we do not over-deglitch the data and do not flag by mistake object structures as glitches by projecting the glitch mask in the sky. In this glitch “map” the distribution of glitches should be discontinuous and the object structure should not be recognisable. A satisfactory setting for the `n σ` parameter of the task is 25-30 which leads to

a glitch rate of less than 1% of the data. We produce final maps using *Scanamorphos*¹⁸ (Roussel, submitted) with its standard settings, as *Scanamorphos* was the best mapmaking software available to us for removing low-frequency drift and reproducing extended emission in PACS data. After this, the median residual backgrounds were measured in $\sim 1\text{-}4$ arcmin wide strips near the edges of the observed regions and outside of the optical discs. These backgrounds were then subtracted from the data.

In each map, north is up, east is left. The pixel size was set to the default value of 1.4 arcsec at $70 \mu\text{m}$ and 2.85 arcsec at $160 \mu\text{m}$, which corresponds to 0.25 times the FWHM of the PSF in typical PACS observations. The PSF has a 3-lobed structure and pronounced Airy rings; the FWHM of the major axis in individual scan maps in these data is 6 arcsec at $70 \mu\text{m}$ and 12 arcsec at $160 \mu\text{m}$ according to the PACS Observer’s Manual from the *Herschel* Space Observatory (2010a)¹⁹. The calibration uncertainty is 10% at $70 \mu\text{m}$ and 20% at $160 \mu\text{m}$ (Poglitsch et al. 2010). Colour corrections and other effects are expected to be small compared to the calibration uncertainty and are thus not included here.

3.1.3 SPIRE 250-500 μm data

The SPIRE observations for each galaxy were performed as a pair of orthogonal scans using a 30 arcsec s^{-1} scan rate and nominal bias voltage settings. The areas covered in the scan maps, again selected to sample an area at least 1.5 times the size of the optical disc, are 40×40 arcmin for M81, 20×20 arcmin for M83, 30×30 arcmin for NGC 2403.

The SPIRE 250-500 μm observations produce timeline data that were processed using a customized version of the official scan map pipeline script (see Griffin et al. (2009) and Dowell et al. (2010) for more information) run in a version of HIPE with the continuous integration build number 4.0.1343, which was the developers’ branch of the data reduction software. This version of the pipeline is similar to the script in the publicly-released version 5 of HIPE, and we also used the new flux calibration product (based on Neptune observations) that was included in version 5.

The first steps of the timeline processing apply concurrent glitch removal (the removal of cosmic rays that affect all detectors in an individual array) and then wavelet glitch removal (the removal of cosmic rays from individual detectors), with the module adjusted to mask 7 samples following a glitch. Next, we applied an electrical low pass filter correction and flux calibration, and then we re-applied the wavelet glitch removal, as, in the version of the software that we were using, an additional deglitching step found to improve the removal of glitches from the data. After this, we applied a time response correction.

We skipped applying the default temperature drift correction and baseline subtraction and instead used a custom method called BriGAdE (Smith et al., in preparation) to remove the temperature drift and bring all bolometers to the same level. For each bolometer in each array, BriGAdE fits a linear function to the relation between the bolometer signal timeline and the array’s thermistor signal timeline after ‘jumps’ (sudden DC offset in the thermistor timelines) have been removed. The timeline fitting is applied to the bolometer data for the whole observation including turnaround data but excluding samples with signals from bright sources or unidentified

¹⁸ Available at <http://www2.iap.fr/users/roussel/herschel/>.

¹⁹ The PACS Observer’s Manual is available at http://herschel.esac.esa.int/Docs/PACS/pdf/pacs_om.pdf.

glitches. For the 250 and 500 μm arrays, where we have two functional thermistors, we used the thermistor providing the best fit to each bolometer. The 350 μm array has only one functional thermistor, and so that thermistor needed to be used for this processing step. The resulting functions, which directly relate the thermistor signal to the background signal (including drift) measured by the bolometers, are then used to calculate and subtract the background signal from each bolometer signal timeline. We have found that this method improves the baseline subtraction significantly, especially in cases where there are strong temperature variations during the observation.

We used the naive mapper in HIPE to create the final maps used in this analysis. We set the pixel size to those listed in Table 2 because they are the smallest pixel sizes possible that do not include significant numbers of map pixels that were not crossed by detectors. We then subtracted the median background levels measured in ~ 4 -6 arcmin wide regions outside the optical discs of the galaxies near the edges of the mapped area. The SPIRE PSFs have FWHM that vary as a function of pixel scale according to the SPIRE Observer’s Manual from the Herschel Space Observatory (2010b)²⁰; Table 2 lists the FWHM for the pixel sizes that we used. By default, the pipeline produces monochromatic flux densities for point sources where νf_ν is constant, so we needed to apply corrections that adjust the monochromatic flux density values from point source to extended source values and colour corrections (see Herschel Space Observatory 2010b, for more information), both of which are also listed in Table 2. The 350 μm data are also multiplied by 1.0066 to correct for an issue related to an update of the filter profile, and the other corrections are based on the updated filter profile. The colour corrections that we use assume that the sources are extended and have dust SEDs that resemble blackbodies modified with emissivity functions that scale as λ^{-2} (which is consistent with Li & Draine 2001). The temperatures are assumed to lie between 15 and 25 K. We compared the slopes of these function at the central wavelengths for each SPIRE band to the slopes in the colour correction tables given by Herschel Space Observatory (2010b) to determine the colour corrections given in Table 2. The final calibration uncertainties in the data include 5% systematic uncertainties that is correlated across all SPIRE bands and 2% random uncertainties in each band (Herschel Space Observatory 2010b).

3.2 Tracer of total stellar emission

As a tracer of the surface brightness of the total stellar population, we used 1.6 μm (H-band) images from the “2MASS Large Galaxy Atlas (Jarrett et al. 2003). These data sample the Rayleigh-Jeans side of the thermal emission from the total stellar populations within galaxies, and they are relatively unaffected by dust extinction. Shorter wavelength data would tend to be strongly affected by dust extinction effects and could be affected more by variations in the ages of the stellar populations. Longer wavelength data, particularly 3.6 μm data from *Spitzer*, is even less affected by dust extinction than the 1.6 μm data. However, multiple recent studies have demonstrated that the 3.6 μm band may sometimes include thermal emission from hot dust at 700-1000 K associated with sites of very strong star formation (Smith & Hancock 2009; Mentuch et al. 2009, 2010). Mentuch et al. (2010) even showed that such emission has been detected in the 3.6 μm images of M81 and NGC 2403.

Furthermore, Flagey et al. (2006) have shown that polycyclic aromatic hydrocarbon spectral feature emission may also contribute up to 50% of the observed emission in the 3.6 μm *Spitzer* band. Hence, the 1.6 μm band appears to be the best band to use for tracing total stellar populations, as it is the best compromise between dust extinction effects and dust emission effects.

The processed, calibrated images were acquired from the NASA/IPAC Extragalactic Database. The 1.6 μm images all have pixel sizes of 1 arcsec pixel⁻¹. The FWHM of the PSF is reported to be 2-3 arcsec (Jarrett et al. 2003); we use 2.5 arcsec for our analysis. The flux calibration uncertainties are 3% (Jarrett et al. 2003). To prepare the images for analysis, we measured median background surface brightnesses in multiple circular regions outside the optical discs of each galaxy and subtracted from each image. We then identified bright foreground stars as unresolved sources with $I_{1.6\mu\text{m}}/I_{24\mu\text{m}} \gtrsim 50$ (using reprocessed 24 μm data from observations originally performed by SINGS and by Engelbracht et al. (2005)) and removed them by interpolating over them.

3.3 Tracer of star formation

We use $\text{H}\alpha$ images of the galaxies as a straightforward tracer of how star formation heats the ISM in these galaxies. These images trace both the photoionised gas in star forming regions themselves as well as diffuse emission from gas that is ionised by photons escaping from the star forming regions while tending not to include emission from other sources. However, the $\text{H}\alpha$ images will be affected by extinction, with the extinction effects expected to be the strongest in star forming regions. This may flatten some of the relations between $\text{H}\alpha$ intensity and other quantities. It would be preferable to use a tracer of star formation that corrects for dust extinction by combining the $\text{H}\alpha$ emission (or emission in another band) with dust emission associated with star formation, such as 24 μm emission. However, these techniques have only been developed for either compact sources within galaxies (Calzetti et al. 2007) or for global flux density measurements (Zhu et al. 2008; Kennicutt et al. 2009). No corrections have been created for diffuse emission within galaxies, and using dust emission in any band to attempt this may be difficult, as even diffuse mid-infrared emission can potentially contain diffuse dust emission heated by evolved stars (e.g. Arendt et al. 1998; Li & Draine 2001) as well as stellar emission. However, analyses with *Spitzer* data have shown that very few $\text{H}\alpha$ sources in nearby spiral galaxies are severely obscured by dust (Prescott et al. 2007), and so even without dust extinction corrections, the $\text{H}\alpha$ data should still perform reasonably well at tracing emission from star forming regions. Although we may expect the data to exhibit some additional scatter without extinction corrections, the uncorrected $\text{H}\alpha$ images are still the most suitable data for tracing how star formation regions heat both compact and diffuse regions.

The $\text{H}\alpha$ images for M81 and NGC 2403 were originally made by Boselli & Gavazzi (2002) using a 1024 \times 1024 CCD with a 0.69 arcsec pixel⁻¹ scale at the 1.20 m Newton Telescope at the Observatoire de Haute Provence. The observations for each galaxy consist of a set of separate pointings that completely cover the optical disk of the galaxy. The observations were performed with interferometric filters where one was an in-band filter and the other was an off-band filter; the $\text{H}\alpha$ image was made by subtracting one image from the other. The FWHM of the PSF was reported to vary between 2 and 4 arcsec; we use 3 arcsec. Calibration uncertainties in the data are 5%. See Boselli & Gavazzi (2002) for additional details.

²⁰ The SPIRE Observer’s Manual is available at http://herschel.esac.esa.int/Docs/SPIRE/pdf/spire_om.pdf.

Table 2. Characteristics of the SPIRE 250–500 μm data and corrections applied to the data.

Wave Band (μm)	Pixel Scale (arcsec)	PSF FWHM (arcsec) ^a	Correction from Point Source to Extended Source Emission ^b	Colour Correction ^b
250	6	18.2	0.9939/1.0113	0.993 ± 0.009
350	8	24.5	0.9920/1.0087	1.000 ± 0.007
500	12	36.0	0.9773/1.0065	1.000 ± 0.008

^a The FWHM in the map data varies with pixel scale. These values are for the pixel scales that we used.

^b These are multiplicative corrections based on the values given by the Herschel Space Observatory (2010b).

The $\text{H}\alpha$ image for M83 was originally made by Meurer et al. (2006) as part of the Survey for Ionization in Neutral Gas Galaxies (SINGG) and was distributed as part of SINGG release 1.0. The observations were performed at the Cerro Tololo 1.5 Meter Telescope using the 2048×2048 CFCCD, which has a plate scale of $0.43 \text{ arcsec pixel}^{-1}$. On- and off-band images were obtained using narrowband filters; the $\text{H}\alpha$ image was made by subtracting the on-band image from the off-band image. The reported median FWHM of the PSF of the survey observations is 1.6 arcsec . Calibration uncertainties are 4%. Additional details are provided by Meurer et al. (2006).

To prepare the $\text{H}\alpha$ images for use in our analysis as a tracer of both the compact and diffuse emission from photoionised gas, we identified foreground stars in the image, which appeared as incompletely subtracted point sources, and also measured and subtracted the median background emission in circular regions at the edges of the images (in the case of M81 and M83) or at the edge of the region with uniform coverage (in the case of NGC 2404). Additionally, for M81, most of the emission within the central $5.7 \times 3.0 \text{ arcmin}$ (approximately the central 3 kpc) of the $\text{H}\alpha$ image originates from either the AGN or incompletely subtracted stellar emission from the bulge; it even has a light profile with artefacts that are similar to the incompletely-subtracted foreground stars. This area is masked out for the analysis. We corrected the $\text{H}\alpha$ measurements for foreground dust extinction within the Milky Way using calculations from the NASA/IPAC Extragalactic Database that are based on data from Schlegel et al. (1998); the R-band extinction values are given in Table 3. We also applied corrections to remove the [NII] line emission; we assume that the [NII]/ $\text{H}\alpha$ ratios are approximately uniform across the discs of the galaxies. The $\text{H}\alpha$ data from Boselli & Gavazzi (2002) contain emission from both the 6548 and 6583 \AA lines, while the data from Meurer et al. (2006) contain emission from only the 6583 \AA line. In the case of M81, we used data on HII regions from Garnett & Shields (1987) to estimate the [NII] (6548 and 6583 \AA)/ $\text{H}\alpha$ ratio to be 0.40 ± 0.13 . For M83, the [NII] (6583 \AA)/ $\text{H}\alpha$ ratio is estimated to be 0.34 based on the data from Boissier et al. (2005). From the radial strip data presented by Moustakas et al. (2010), we calculated the [NII] (6548 and 6583 \AA)/ $\text{H}\alpha$ ratio for NGC 2403 to be 0.28 ± 0.05 .

3.4 Convolution and binning

To compare images from different wave bands without worrying about beam effects, it is necessary to match the PSFs of all of the data to the PSF of the wave band with the lowest resolution. Otherwise, the analysis will be strongly affected by variations related

Table 3. Foreground extinction values used to correct $\text{H}\alpha$ fluxes.

Galaxy	A_R^a
M81	0.214
M83	0.176
NGC 2403	0.077

^a These values were calculated by the NASA/IPAC Extragalactic Database using data from Schlegel et al. (1998). These extinction values are only for the foreground and do not include extinction within the target galaxies.

to PSF shapes, with side lobes appearing around bright sources in maps based on surface brightness ratios and with fainter regions appearing biased towards emission from the wave bands with the broader PSFs. For our analysis, we matched the PSFs of the data to the PSF of the 500 μm data, which has a FWHM of 36.0 arcsec in the maps.

The SPIRE PSFs are very close to Gaussian (i.e. the Airy rings are weak compared to the peak of the PSF), so we could use the equation

$$K(r) = e^{-r^2/2(\sigma_2^2 - \sigma_1^2)} \quad (2)$$

to create a convolution kernel $K(r)$ that could be used to match the PSF of data with a width σ_1 to a PSF with a width of σ_2 . However, the MIPS 70 μm data and the PACS 70 and 160 μm data have strong Airy rings, and applying this procedure would leave rings around bright sources. To correct for this, we created convolution kernels following the procedure given by Gordon et al. (2008) (and also see Bendo et al. (2010a)). We used

$$K = F^{-1} \left[\frac{W(\omega)F[PSF_2]}{F[PSF_1]} \right] \quad (3)$$

to create convolution kernels K to match PSF_1 to PSF_2 . F is a Fourier transform and $W(\omega)$ is a radial Hanning truncation function given by

$$W(\omega) = \begin{cases} \frac{1}{2} \left[1 + \cos \left(\frac{2\pi\omega}{\omega_0} \right) \right] & \omega \leq \omega_0 \\ 0 & \omega > \omega_0 \end{cases} \quad (4)$$

that is used to suppress high-frequency spatial noise in the resulting kernels by adjusting ω_0 . For the MIPS 70 μm PSF, we used radially-smoothed versions of the empirical PSFs originally presented in Young et al. (2009). For the PACS PSFs, we used radially-smoothed versions of the sum of three PSFs made from Vesta data

(see Lutz 2010, for more information)²¹. For the other PSFs, we used Gaussian functions.

For quantitative analyses, we rebinned the data into 36 arcsec pixels and then measured surface brightnesses or intensities in all pixels where we detected emission at the 5σ level or higher in the 70–500 μm bands. We used this bin size because it is equivalent to the FWHM of the PSF in the convolved data, and so we will avoid having multiple pixels sampling the PSF of a single point-like source. The coordinates of the bins were set up so that the centre of each galaxy would fall within the centre of a pixel. This binning procedure has an advantage over either measuring surface brightnesses in regions identified by eye or measuring surface brightnesses in regions identified in a specific wave band in that it will be unbiased towards any specific type of region and therefore will include both emission from point-like sources and the diffuse ISM. An example of the resulting convolved and binned data is shown in Figure 4. In our analysis, we use measurements in 322 bins for M81, 158 bins for M83, and 179 bins for NGC 2403. Note that we did not use the central 36 arcsec square bin in M81 for analysis because it includes emission from the AGN, although we do display this data point in our figures.

4 ANALYSIS

4.1 Colour temperature maps

Figures 5–7 show the colour temperatures based on the surface brightness ratios produced by this analysis. The colour temperatures are calculated using

$$\frac{I_\nu(\lambda_1)}{I_\nu(\lambda_2)} = \left(\frac{\lambda_2}{\lambda_1}\right)^{3+\beta} \left(\frac{e^{hc/\lambda_2 kT} - 1}{e^{hc/\lambda_1 kT} - 1}\right) \quad (5)$$

in which dust emission is treated as originating from a single component that is optically-thin in the far-infrared. The parameter β is the dust emissivity coefficient that indicates how the emissivity scales as a function of wavelength. We use $\beta = 2$ (given by Li & Draine 2001) for this calculation, as it has previously been shown to accurately describe the observed emissivity of dust. The colour temperature maps for each galaxy look notably different in comparison to the stellar and dust structures in Figures 1–3. The emission in some bands, particularly the shorter wavelength ones, may originate from dust with a range of temperatures. Moreover, temperatures determined from the Rayleigh-Jeans side of the SED may be improperly constrained without using data from the Wien side of the peak. Hence, these colour temperatures should be used to aid in relating the colour variations in the maps to the SED shape and should not necessarily be interpreted as the physical dust temperatures, even though this could be the case for the colour temperatures based on the longer wavelength bands. Also, the 350/500 μm colour temperatures tend to appear noisier. Both wave bands sample locations on the Rayleigh-Jeans tail of the dust SED and are therefore relatively less sensitive to temperature variations, which causes the images to appear noisy.

The M81 colour temperature maps are simply modified versions of the ratio maps published by Bendo et al. (2010b). The 70/160 μm colour temperatures and, to a limited degree, the

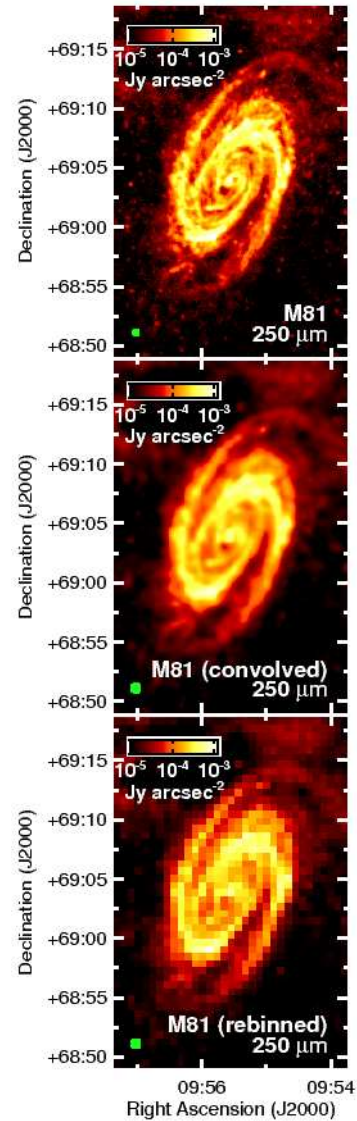


Figure 4. The original 250 μm image of M81 (top), the 250 μm image after it has been convolved with a kernel to match the PSF to that of the 500 μm data (middle), and the convolved 250 μm image after rebinning (bottom). The green circles show the FWHM of the PSF of the data. In the convolved and rebinned maps, this PSF is 36 arcsec, which is also the size of the bins. Each map is 30×20 arcmin with north up and east to the left.

160/250 μm colour temperatures are enhanced in the spiral arms. However, the 160/250 μm , 250/350 μm , and 350/500 μm colour temperature maps appear to be dominated by radial variations in the colour temperatures. This implies that the colour variations between 160 and 500 μm are dependent either on galactocentric radius or on stellar surface brightness.

The M83 colour temperature maps show enhancements near the nucleus and along spiral arms near star forming regions. The structures traced in the 70/160 μm and 160/250 μm colour temperature maps clearly trace $\text{H}\alpha$ regions along the edges of the spiral arms instead of the stellar structures seen in the 1.6 μm image, suggesting that these colour temperatures are linked to star formation activity. We observe these structures on the leading edges of both spiral arms, which demonstrates that the structures are not simply the result of a misalignment in astrometry between two

²¹ These data are available at http://ftp.sciops.esa.int/pub/hsc-calibration/PACS/PSF/PACSPSF_PICC-ME-TN-033_v1.0.tar.gz. The documentation is available from <http://herschel.esac.esa.int/twiki/pub/Public/PacsCalibrationWeb/bolopsfv1.01.pdf>.

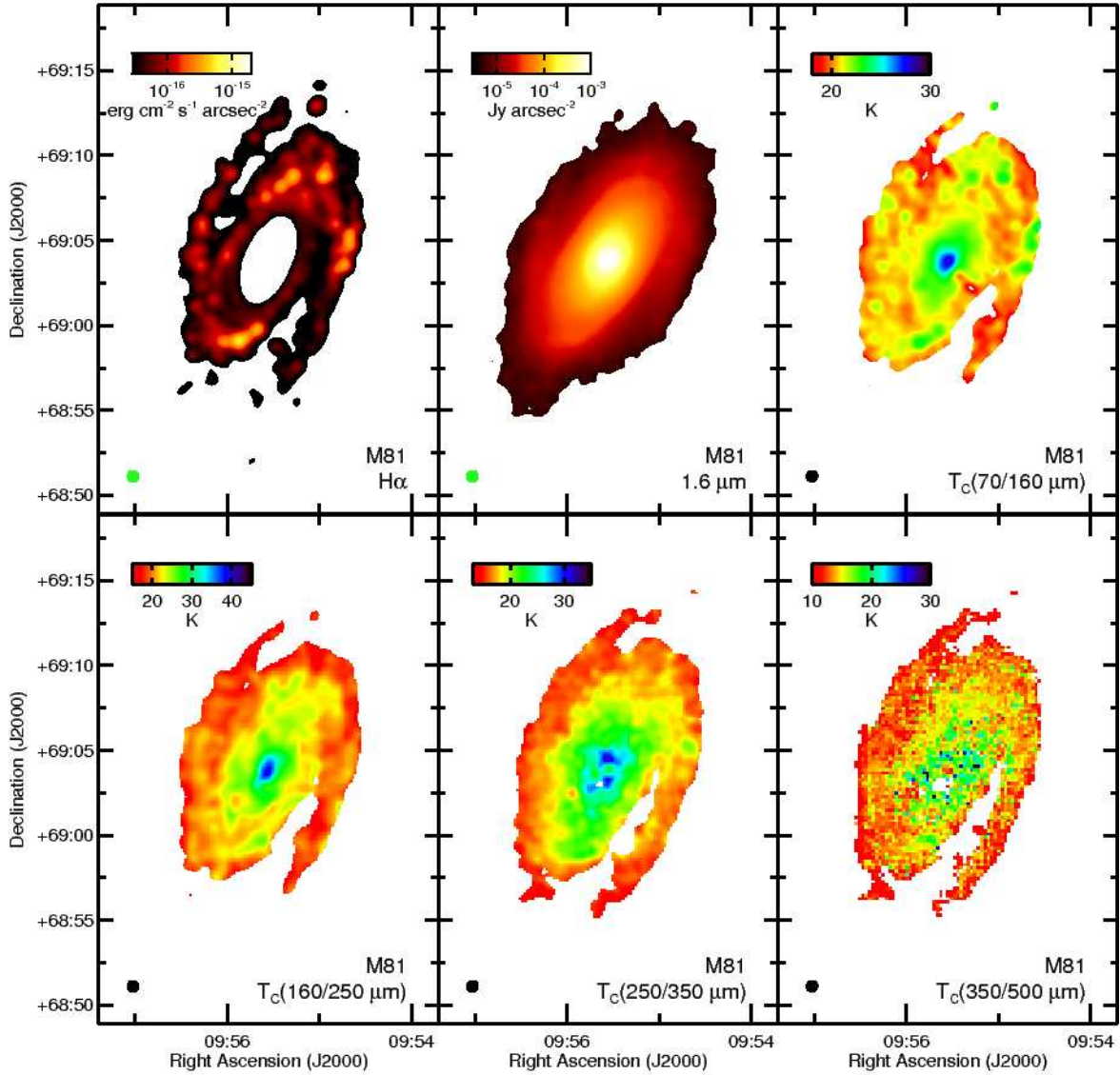


Figure 5. The colour temperature maps of M81 and $H\alpha$ and $1.6\ \mu\text{m}$ images at the same resolution. All of these maps were created from data where the PSF was matched to the PSF of the $500\ \mu\text{m}$ data, which has a FWHM of $36\ \text{arcsec}$ (shown by the black circles in the lower left corner of each panel). This $36\ \text{arcsec}$ circle is also the same width as the bins used in the analysis in Sections 4.2 and 4.3. Pixels where the signal was not detected at the 5σ level in either the single band shown (in the case of the $H\alpha$ and $1.6\ \mu\text{m}$ images) or in both bands (in the case of the colour temperature maps) were left blank (white). Each map is $30 \times 20\ \text{arcmin}$, and north is up and east is left in each panel.

pairs of images. The relatively smooth gradient in the $250/350\ \mu\text{m}$ colour temperature is consistent with the gradient in the $1.6\ \mu\text{m}$ maps, and the central region with $250/350\ \mu\text{m}$ colour temperatures above 30K , while very noisy, appears to correspond roughly to the bar seen in the $1.6\ \mu\text{m}$ image. This suggests that the $250/350\ \mu\text{m}$ colour temperatures could be affected by heating by the total stellar population. Foyle et al. (in preparation) are performing an analysis that more carefully examines the colour gradients across the arms and the bar. While the nucleus itself appears to have enhanced $70/160\ \mu\text{m}$ colour temperatures, the regions with the most strongly enhanced colour temperatures in the other bands are the regions just to the east and west of the nucleus. The reason for this is unclear. One possibility is that the PSF matching is imperfect and residual side lobes have appeared around the very bright nucleus in some of the data. However, such artefacts are not seen for other

sources processed in the same way; see, for example, VS 44 in NGC 2403. Another possibility is that some of the dust in the nucleus itself is relatively cold because the dust shields itself from the nuclear starburst, but the regions immediately outside the nucleus are not as well shielded and thus become warmer in all wave bands. The nuclear colour temperature structure is poorly resolved in the resolutions that we are working at and the structures are relatively sensitive to $1\text{--}2\ \text{arcsec}$ adjustments in astrometry (although the binned data are unaffected by such adjustments), so it is difficult to accurately assess this with the data in hand. Future work with higher-resolution data is warranted.

The NGC 2403 colour temperature maps show significant differences in the dust heating between 70 and $500\ \mu\text{m}$. The $70/160\ \mu\text{m}$ colour temperature map shows temperature enhancements mainly at locations with bright star forming regions. How-

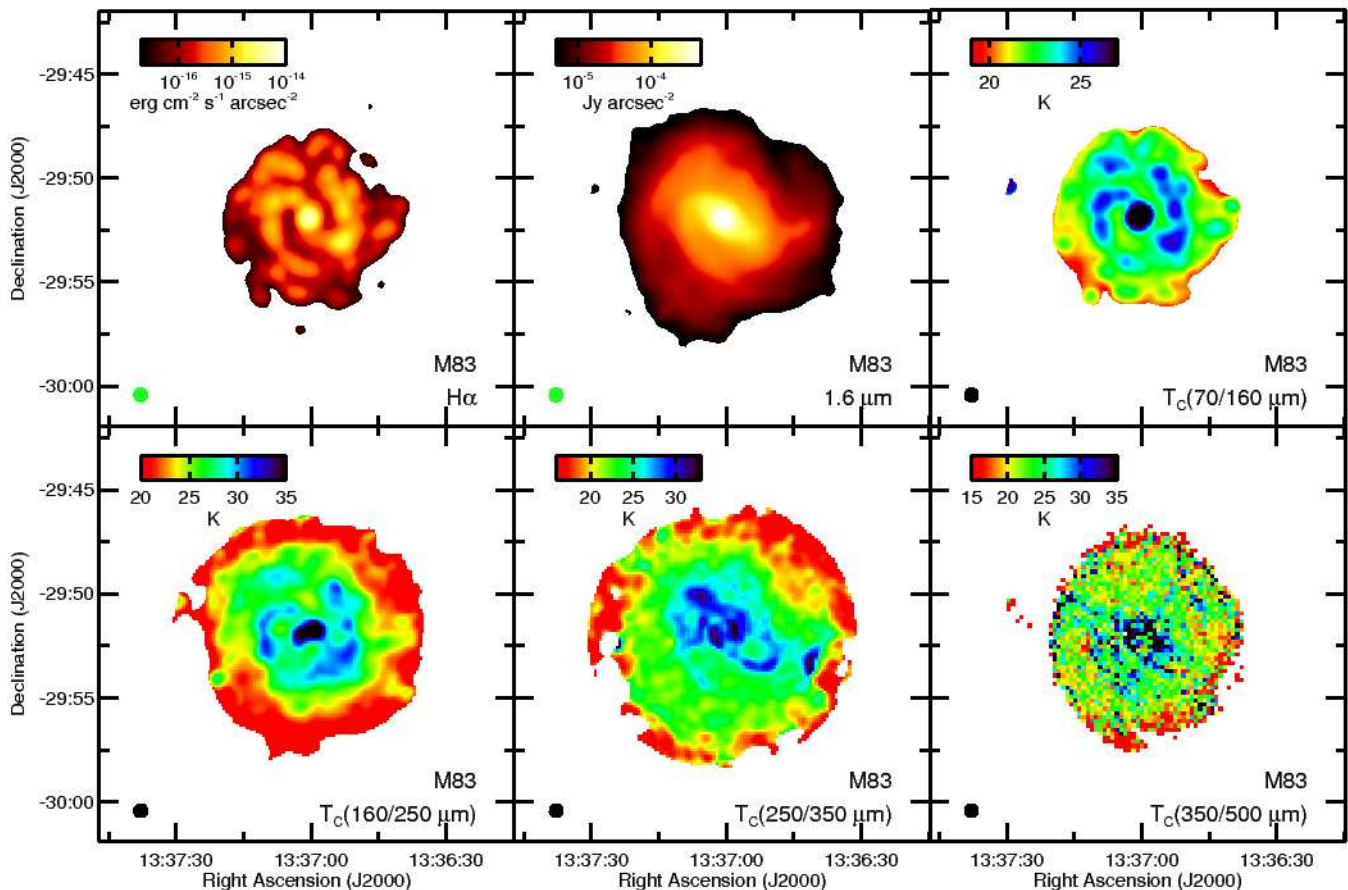


Figure 6. The colour temperature maps of M83 and H α and 1.6 μ m images at the same resolution. Each map is 20 \times 20 arcmin. See the caption of Figure 5 for other information about the layout.

ever, these regions become much less prominent in the colour temperatures based on longer wavelengths. In the 160/250 μ m and 250/350 μ m colour temperature maps, the centre of the galaxy is approximately as warm as VS 44 (the bright star forming region to the northeast of the centre), and smooth radial variations generally become more prominent than localised dust temperature enhancements near star forming regions. The 350/500 μ m map appears to be similar, although the map is so noisy that it is difficult to discern any structures. Overall, these maps suggest that heating by star forming regions is important between 70 and 350 μ m but that variations dependent on either total stellar surface brightness or radius becomes more important when proceeding to wavelengths longer than 160 μ m, even though the dust structures themselves appear associated with the structures seen in H α .

Overall, the three galaxies show similar trends. In the colour temperatures based on the shortest wavelength data, the temperatures appear strongly enhanced in regions with star forming regions, but in colour temperatures based solely on the >250 μ m data, the variations in the colour temperatures appear more strongly related to either total stellar surface brightness or radius. This suggests a scenario in which star forming regions are located within dust clouds that are optically thick to the blue and ultraviolet light from star forming regions. In this scenario, the star forming regions would only heat a small fraction of the total dust mass in these clouds, and this warmer dust would be the predominant emission source at < 160 μ m. However, most of the dust on the outside

of these clumps as well as the dust in the diffuse ISM would be shielded from the ultraviolet and blue light from star forming regions and would instead be heated by the diffuse interstellar radiation field. While this dust would be cooler, the greater mass fraction of this cooler component would make it the more dominant emission source on the Rayleigh-Jeans side of the dust SED at > 250 μ m.

These imaging data have shown significant qualitative differences between the dust heating as a function of wavelength. In the following sections, we will examine the different trends further using quantitative analyses based on the binned data.

4.2 Comparisons of surface brightness ratios to 1.6 μ m emission

Figure 8 shows how the surface brightness ratios for 36 arcsec square subregions vary versus 1.6 μ m surface brightness, which effectively traces the starlight from the total stellar populations within these galaxies. Statistical information on the relations is given in Table 4.

Interestingly, strong correlations can be seen between the 1.6 μ m surface brightness and the 160/250 μ m, 250/350 μ m, and 350/500 μ m ratios for all three galaxies. In almost all cases, the correlation coefficients are above 0.70. The squares of the correlation coefficients indicate the variance in one quantity that can be related to the best fitting linear function to the other quantity. In this

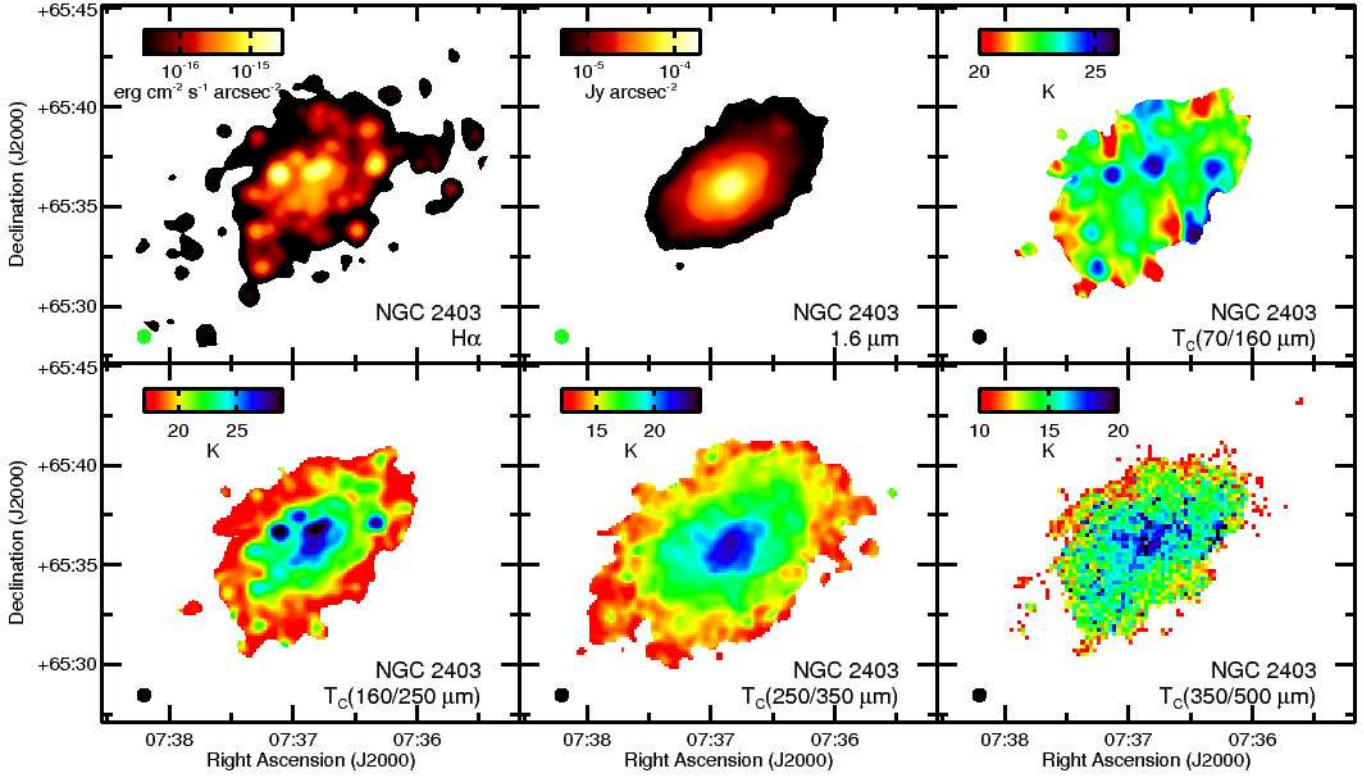


Figure 7. The colour temperature maps of NGC 2403 and H α and 1.6 μ m images at the same resolution. Each map is 21×18 arcmin. See the caption of Figure 5 for other information about the layout.

Table 4. Results from fits between surface brightness ratios and 1.6 μ m surface brightness.

Galaxy	Surface Brightness Ratio	Slope ^a	Correlation Coefficient ^a
M81	70/160 μ m	0.241 ± 0.002	0.65
	160/250 μ m	0.142 ± 0.004	0.87
	250/350 μ m	0.088 ± 0.005	0.92
	350/500 μ m	0.067 ± 0.007	0.81
M83	70/160 μ m	0.3456 ± 0.0011	0.82
	160/250 μ m	0.1137 ± 0.0005	0.79
	250/350 μ m	0.0362 ± 0.0006	0.83
	350/500 μ m	0.0474 ± 0.0011	0.64
NGC 2403	70/160 μ m	0.023 ± 0.002	0.32
	160/250 μ m	0.120 ± 0.002	0.85
	250/350 μ m	0.074 ± 0.002	0.92
	350/500 μ m	0.047 ± 0.003	0.72

^a These quantities are for the relations describing the logarithm of the surface brightness ratios as a function of the logarithm of the 1.6 μ m surface brightness in Jy arcsec⁻². The fits are weighted by the uncertainties in the x- and y- values.

context, at least 50% and often above 80% of the variance in the surface brightness ratios can be related to the stellar surface brightness. The 350/500 μ m ratios for the three galaxies show more scatter (i.e. have lower correlation coefficients) than the 250/350 μ m ratios in the relations with 1.6 μ m surface brightness. This could

be because of the relatively high uncertainties in the ratios, which are in part a consequence of sampling data on the Rayleigh-Jeans tail of the SED where temperature variations have a relatively small effect on the colours. Additionally, the nucleus of M81 (which corresponds to the data point with the highest 1.6 μ m surface brightness) deviates significantly from the relations between the 1.6 μ m surface brightness and either the 250/350 μ m or 350/500 μ m ratios. As stated by Bendo et al. (2010b), this is probably because the AGN produces non-thermal emission at submillimetre wavelengths (Markoff et al. 2008), and it was not included in the derivations of the statistical results shown in Table 8. None the less, the overall results indicate that the total stellar populations in each galaxy play a significant role in locally heating the dust that is emitting at >160 μ m. Such a result may be expected in M81, where the bulge has a significantly higher surface brightness in visible light compared to the disc and where dust heating could be expected to be dominated by evolved stars. However, it is surprising that this strong correlation is seen in NGC 2403, where the bulge is either very faint or non-existent.

The results for the correlations between the 70/160 μ m ratios and the 1.6 μ m surface brightness, however, show that dust heating by the total stellar population may not be as important, although this varies among the three galaxies examined here. Weak correlations are seen in M81; less than 50% of the variance in the ratio is related to the stellar surface brightness. A relation may be present where the 1.6 μ m surface brightness is higher than 10^{-4} Jy arcsec² in M81, but the relation flattens out for fainter regions. This could indicate that the bulge plays a role in heating the dust

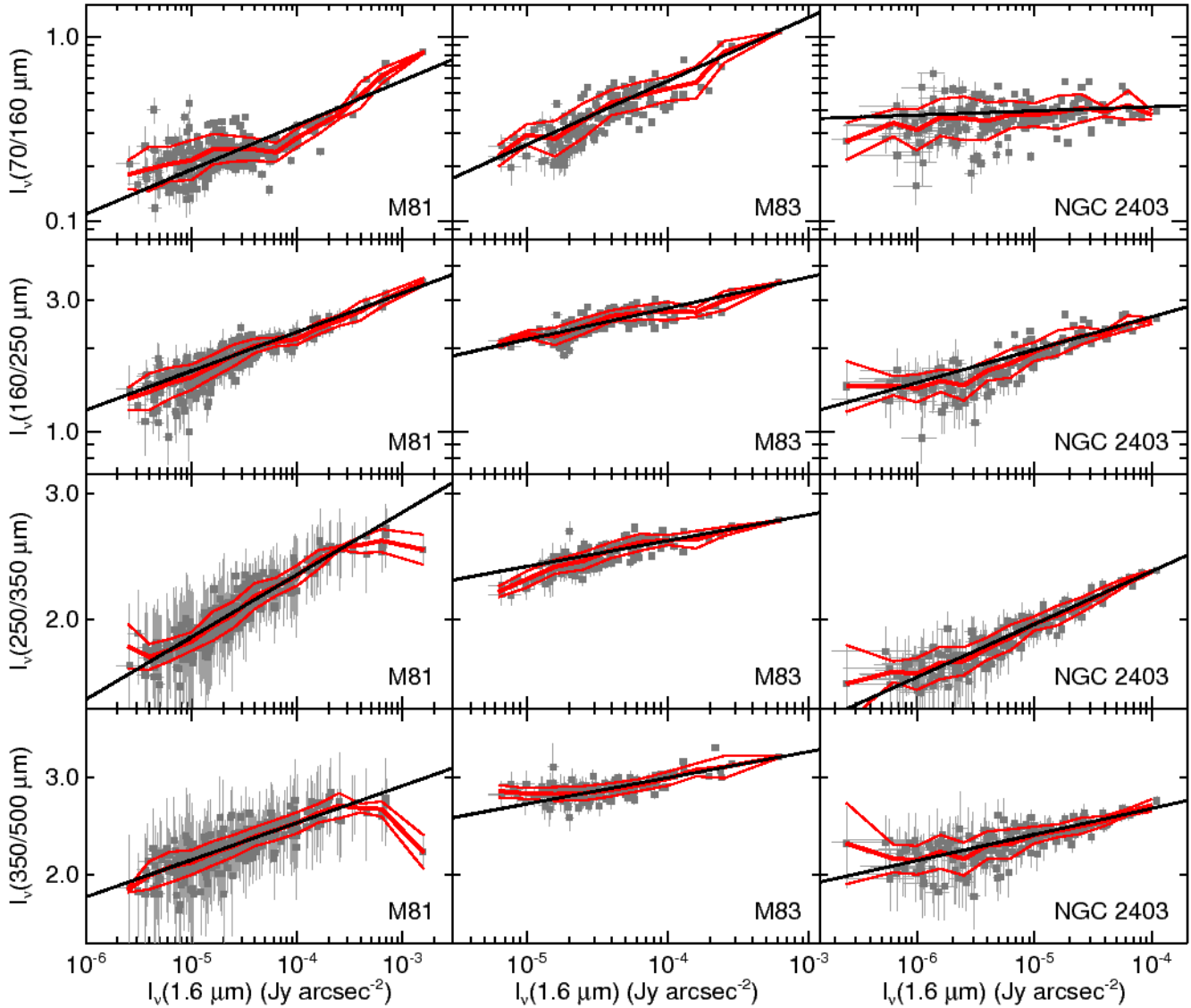


Figure 8. Comparisons of the surface brightness ratios to the $1.6 \mu\text{m}$ surface brightnesses for the 36 arcsec square subregions in the sample galaxies. The solid lines show the best fit lines. The thick red line shows the weighted mean of the ratios averaged over intervals with a width of 0.2 in $\log(I_\nu(1.6 \mu\text{m}))$, and the thinner red lines show the weighted standard deviation of the data (except when one data point falls within an interval, in which case the uncertainty in the data point is used). Parameters related to the fits are shown in Table 4.

that produces the $70 \mu\text{m}$ emission, but only in the centre where the bulge is very bright. The correlation coefficient for the relations between the $70/160 \mu\text{m}$ ratio and $H\alpha$ (discussed in Section 4.3) is higher for M83, and the $70/160 \mu\text{m}$ colour temperature map for M83 shows that the regions with enhanced temperatures correspond to $H\alpha$ sources, which suggests that the relation seen between the $70/160 \mu\text{m}$ ratio and $1.6 \mu\text{m}$ surface brightness is partly a consequence of the correlation between the stellar structures and the structures tracing star formation. As for NGC 2403, the correlation between the $70/160 \mu\text{m}$ ratio and $1.6 \mu\text{m}$ surface brightness is negligible, which reflects the weak influence of the total stellar population on the colour temperatures, as we also inferred from Figure 7.

Bendo et al. (2010b) noted that the far-infrared surface brightness ratios for M81 were correlated with radius. This result was used to infer that the ratios depended on the total stellar surface brightness, which varies with radius within nearby galaxies. For completeness, we re-examined the relations for all three galaxies in this study. Figure 9 shows how the surface brightness ratios for the 36 arcsec square subregions vary versus deprojected galactocentric radius, and Table 5 gives statistical information on these relations. Visually, the relations between radius and either the $160/250 \mu\text{m}$, $250/350 \mu\text{m}$, or $350/500 \mu\text{m}$ ratios appear almost as strong as the relations between $1.6 \mu\text{m}$ surface brightness and these ratios. This is mainly because the stellar surface brightness itself is correlated with radius. However, the correlation coefficients of the trends for

Table 5. Results from fits between surface brightness ratios and deprojected galactocentric radius.

Galaxy	Surface Brightness Ratio	Slope ^a	Correlation Coefficient ^a
M81	70/160 μm	-0.0480 ± 0.0005	-0.57
	160/250 μm	-0.0268 ± 0.0007	-0.82
	250/350 μm	-0.0164 ± 0.0009	-0.92
	350/500 μm	-0.0121 ± 0.0013	-0.80
M83	70/160 μm	-0.1122 ± 0.0003	-0.77
	160/250 μm	-0.0331 ± 0.0001	-0.76
	250/350 μm	-0.0112 ± 0.0002	-0.75
	350/500 μm	-0.0142 ± 0.0003	-0.66
NGC 2403	70/160 μm	-0.0084 ± 0.0007	-0.26
	160/250 μm	-0.0350 ± 0.0006	-0.89
	250/350 μm	-0.0221 ± 0.0006	-0.89
	350/500 μm	-0.0157 ± 0.0010	-0.80

^a These quantities are for the best fit line describing the logarithm of the surface brightness ratios as a function of deprojected galactocentric distance in kpc. The slope has units of dex kpc⁻¹.

the relation with 1.6 μm surface brightness have slightly higher absolute values for all of the M81 relations, three of the relations for M83, and two of the NGC 2403 relations. Moreover, the radial profiles for M81 depart from the best fit lines in the central 2 kpc in a way that would be consistent with heating by bulge stars in this region. Furthermore, the colour temperature maps in Figures 5-7 show the presence of some non-axisymmetric structures that correspond to spiral arms or filaments in each of the galaxies. Some of these features correspond to locations with star forming regions, which can be thought of as also enhancing the total stellar surface brightness. Other features correspond to structures in the 1.6 μm image that are more clearly cases where the surface brightness of the total stellar population increases. Hence, it would make more sense to infer that the surface brightness ratios are more strongly dependent on stellar surface brightness than radius.

Physically, a relation between stellar surface brightness and dust colours is more straightforward than a relation between galactocentric radius and dust colours. The stars can directly heat the dust, so the stellar surface brightness would be directly linked to dust temperature (and hence the surface brightness ratios) regardless of the relation between stellar surface brightness and radius. However, to link the dust temperature with radius without connecting dust temperature to stellar surface brightness is very difficult. We therefore conclude that the correlations between galactocentric radius and either the 160/250 μm , 250/350 μm , or 350/500 μm ratio actually reflect radial variations in the starlight heating the dust.

Figure 10 shows how the 70-500 μm surface brightnesses for the 36 arcsec square subregions are related to the 1.6 μm surface brightnesses. This comparison shows how the dust emission may be related to the distribution of the total stellar population. Good correlations, with coefficients above 0.89, are found between the dust and stellar emission for M83, which we expected, as the infrared and stellar emission appear qualitatively similar. Surprisingly good correlations, with correlation coefficients above 0.85, are found between dust and stellar emission in NGC 2403 despite the significant differences in the appearance of the stellar and dust emission. However, both the stellar and dust emission generally decreases with galactocentric radius, which could cause the stellar emission to appear correlated overall with the dust emission. In contrast to the other two galaxies, the relations between stellar and dust emission

Table 6. Results from fits between far-infrared and 1.6 μm surface brightnesses.

Galaxy	Infrared Surface Brightness	Slope ^a	Correlation Coefficient ^a
M81 ^b	70 μm	0.4164 ± 0.0015	0.78
	160 μm	0.1946 ± 0.0019	0.69
	250 μm	0.115 ± 0.003	0.52
	350 μm	0.077 ± 0.004	0.34
	500 μm	0.048 ± 0.006	0.15
M83	70 μm	1.19 ± 0.05	0.90
	160 μm	0.84 ± 0.03	0.91
	250 μm	0.9284 ± 0.0015	0.90
	350 μm	0.8745 ± 0.0014	0.90
	500 μm	0.7925 ± 0.0018	0.89
NGC 2403	70 μm	0.8038 ± 0.0016	0.88
	160 μm	0.649 ± 0.003	0.90
	250 μm	0.5476 ± 0.0018	0.89
	350 μm	0.462 ± 0.002	0.87
	500 μm	0.389 ± 0.003	0.87

^a These quantities are for the relations for the logarithms of the surface brightnesses in Jy arcsec⁻².

in M81 is fairly good at 70 and 160 μm but worsens towards longer wavelengths. Emission in the 70 and 160 μm bands is more sensitive to variations in dust temperature, and since these bands partly trace dust within M81 that appears to be heated by the stars seen at 1.6 μm , the 70 and 160 μm emission is correlated with the 1.6 μm emission. However, variations in the 350 or 500 μm emission may be more dependent on dust surface density than dust temperature, and so these wave bands appear more poorly correlated with the stars in M81 because the stellar mass is distributed differently from the dust mass.

Although we have found that the distribution of dust and stellar emission may match in many circumstances, this alone does not necessarily indicate that the dust traced in these wave bands is heated by the total stellar population. Dust emission in a single wave band is a function of both dust temperature and dust surface density. For example, it is possible for dust emission at 70 μm in NGC 2403 to appear correlated with 1.6 μm emission even though the colour temperature map and the analysis of the surface brightness ratios suggest that the dust is not heated by the total stellar population. Instead, the dust and stellar surface densities are both correlated with radius in this galaxy, causing the 70 μm emission to appear related to 1.6 μm emission. Conversely, it is possible for dust emission in a single wave band, such as the 500 μm data for M81, to appear uncorrelated with stellar surface brightness because the wave band is more strongly affected by dust surface density variations than dust temperature variations and because the dust and stellar mass is distributed differently within the galaxy. None the less, this does not preclude the possibility that the dust is heated primarily by the total stellar population, thus causing the temperature of the dust to be dependent upon the stellar surface brightness.

4.3 Comparisons of colour temperatures to star formation

Figure 11 shows how the colour temperatures for 36 arcsec square subregions vary versus H α intensity, which traces the star formation within the galaxies. The statistics from these relations are given in Table 7. Each of the galaxies in this analysis give intriguingly dif-

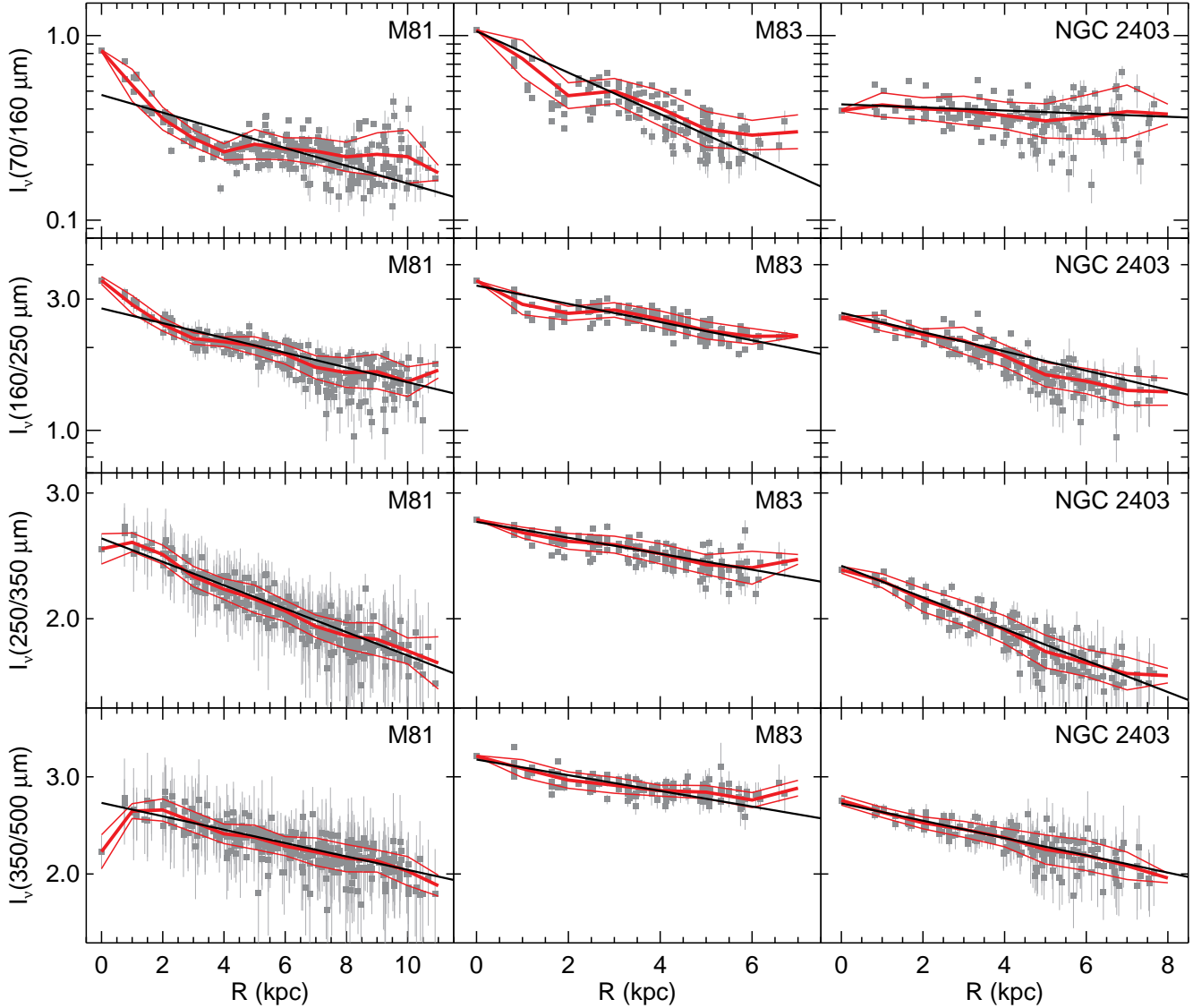


Figure 9. Comparisons of the surface brightness ratios to deprojected galactocentric radius for the 36 arcsec square subregions in the sample galaxies. The solid lines show the best fit lines. The thick red line shows the weighted mean of the ratios averaged over intervals with a width of 1 kpc, and the thinner red lines show the weighted standard deviation of the data (except when one data point falls within an interval, in which case the uncertainty in the data point is used). Parameters related to the fits are shown in Table 5.

ferent results, especially when the results are compared with those data shown in Figure 8 and Table 4.

The data for M81 show that the surface brightness ratios are generally poorly correlated with $H\alpha$ intensity. This is also borne out by the general absence of spiral structure in the colour temperature maps in Figure 5; the colour temperatures primarily vary with radius, and, with the exception of $T_C(70/160 \mu\text{m})$, the spiral structure is very weakly enhanced in the spiral arms if it is enhanced at all. It is possible, however, that the $70/160 \mu\text{m}$ surface brightness ratio is enhanced in star forming regions in the spiral arms, as the regions appear relatively bright in the colour temperature map and as some of the data with the highest $H\alpha$ values in Figure 11 do appear to show a relation with the $70/160 \mu\text{m}$ ratio. However, the central

~ 3 kpc of M81, which is devoid of star formation and which has low $H\alpha$ intensities (although incompletely-subtracted continuum emission from the bulge is seen in the $H\alpha$ image) exhibits higher $70/160 \mu\text{m}$ ratios, demonstrating that the evolved stellar population must be the heating source for the dust emitting at $70 \mu\text{m}$ in this region. As for the other surface brightness ratios, the stronger correlations between the ratios and $1.6 \mu\text{m}$ surface brightness clearly show that the total stellar population plays a much larger role than the star forming regions in heating the dust in M81.

For M83, the correlation coefficients for the relations between $H\alpha$ intensity and either the $70/160 \mu\text{m}$ or $160/250 \mu\text{m}$ ratios is slightly higher than for the corresponding relations with $1.6 \mu\text{m}$ surface brightness, but the correlation coefficient for the $H\alpha$ in-

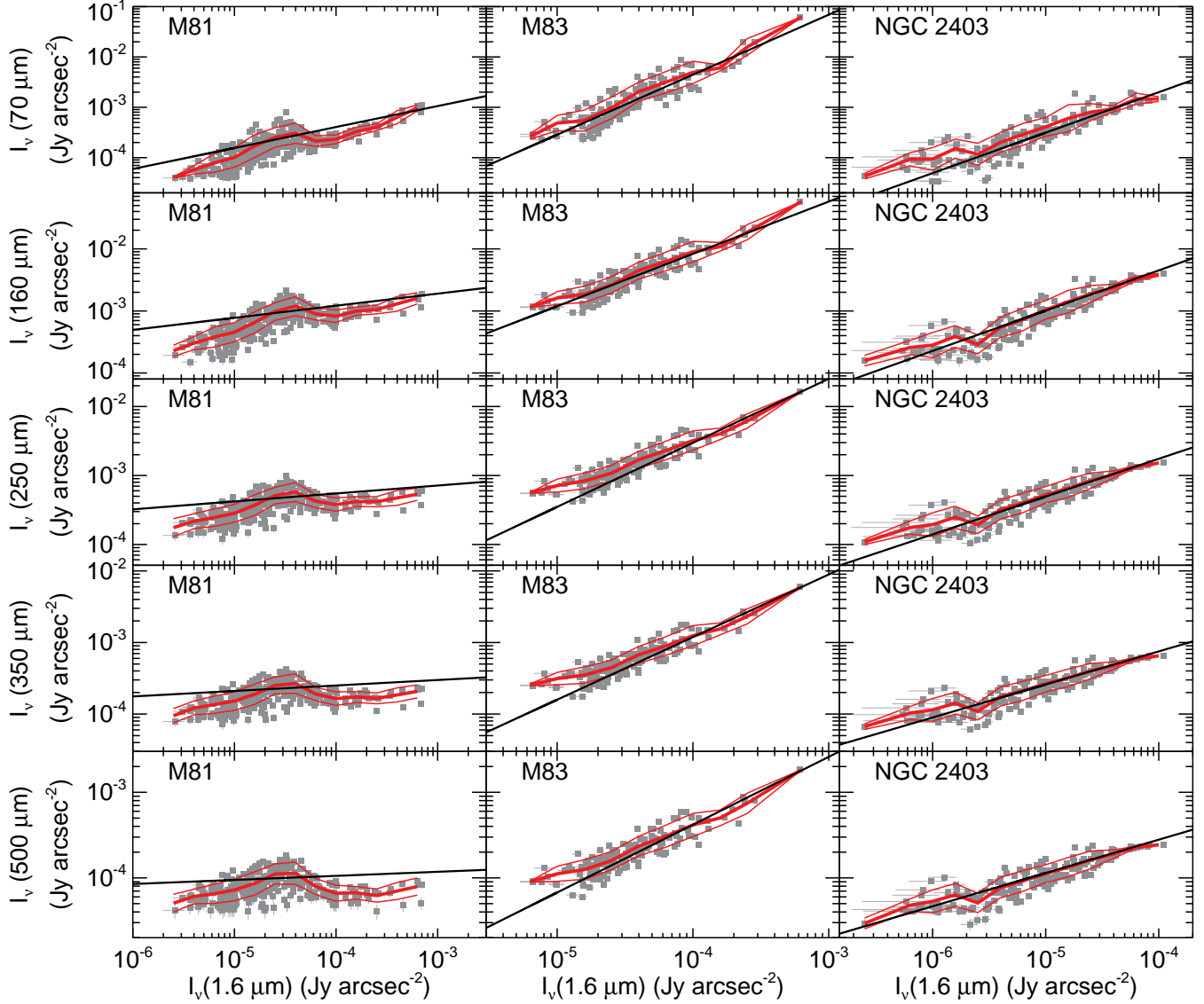


Figure 10. Comparisons of infrared surface brightnesses in individual wave bands to the $1.6 \mu\text{m}$ surface brightnesses for the 36 arcsec square subregions in the sample galaxies. The solid lines show the best fit lines. The thick red line shows the weighted mean of the ratios averaged over intervals with a width of 0.2 in $\log(I_{\nu}(1.6 \mu\text{m}))$, and the thinner red lines show the weighted standard deviation of the data (except when one data point falls within an interval, in which case the uncertainty in the data point is used). Parameters related to the fits are shown in Table 6.

tensity and either the $250/350 \mu\text{m}$ or $350/500 \mu\text{m}$ ratios is lower than the corresponding relations with $1.6 \mu\text{m}$ surface brightness. For the $70/160 \mu\text{m}$, $160/250 \mu\text{m}$, and $250/350 \mu\text{m}$ ratios, the coefficients for the relations with $\text{H}\alpha$ intensity are within 0.10 of the coefficients for the relations with $1.6 \mu\text{m}$ surface brightness. This implies that both $1.6 \mu\text{m}$ and $\text{H}\alpha$ emission correlate with dust temperatures almost equally well. This could be true for a couple of reasons. First of all, the $\text{H}\alpha$ and $1.6 \mu\text{m}$ emission both trace very similar spiral structures within M83 and are correlated with each other to some degree, especially when the data are binned up as we have done here. Hence, even if $\text{H}\alpha$ or $1.6 \mu\text{m}$ emission trace completely different stellar populations, a relation found between either band and far-infrared colours may naturally apply to

the other band as well. It is also possible that both star forming regions and evolved stars heat the dust observed in the far-infrared, with evolved stars responsible for a slightly greater fraction of the heating for dust emitting at longer wavelengths and star forming regions heating more dust at shorter wavelengths. A third possibility is that the $1.6 \mu\text{m}$ band includes a significant contribution from young star-forming regions. However, the spiral structure in the $1.6 \mu\text{m}$ image is not as strong as the structure in the $\text{H}\alpha$ image, and both the $1.6 \mu\text{m}$ and $T_C(250/350 \mu\text{m})$ images exhibit bar structures that do not have such apparent counterparts in either the $\text{H}\alpha$, $T_C(70/160 \mu\text{m})$, or $T_C(160/250 \mu\text{m})$ images, implying that “contamination” of the $1.6 \mu\text{m}$ band by young stars cannot be the

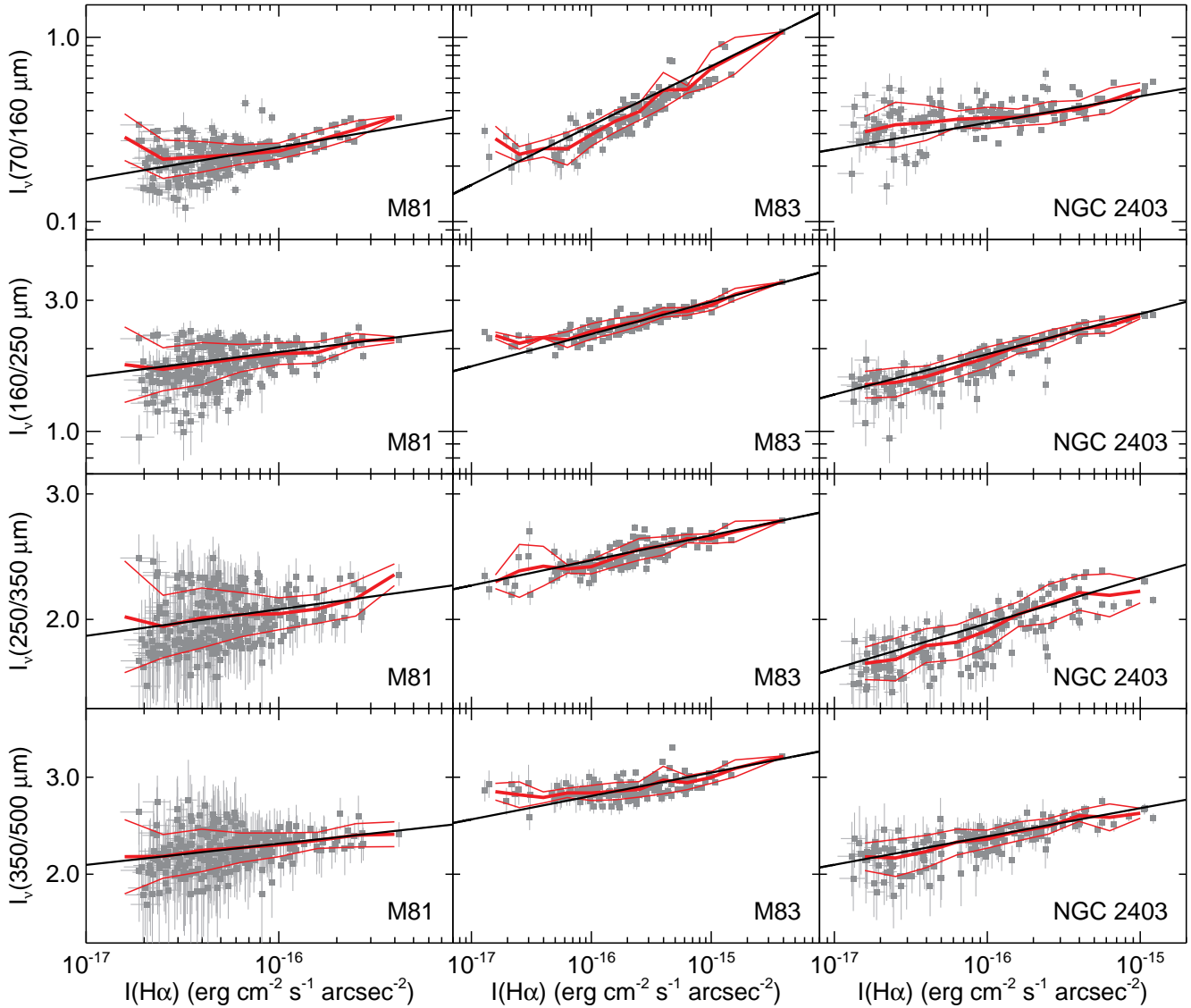


Figure 11. Comparisons of the surface brightness ratios to the $H\alpha$ intensities for the 36 arcsec square subregions in the sample galaxies. The solid lines show the best fit lines. The thick red line shows the weighted mean of the ratios averaged over intervals with a width of 0.2 in $\log(I(H\alpha))$, and the thinner red lines show the weighted standard deviation of the data (except when one data point falls within an interval, in which case the uncertainty in the data point is used). Data from the inner central 5.7×3.0 arcmin (approximately the central 3 kpc) of M81 are not included in the analysis, as it primarily includes incompletely-subtracted continuum emission from the bulge. Parameters related to the fits are shown in Table 7.

only explanation for the similarities in the correlations of surface brightness ratios with either 1.6μ or $H\alpha$ emission.

The results for NGC 2403 are similar to M83 in that the $70/160 \mu$ are clearly more strongly correlated with $H\alpha$ intensity but the $250/350 \mu$ surface brightness ratio is more strongly correlated with 1.6μ surface brightness, with the correlation coefficients for the relations between the $160/250 \mu$ ratio and either $H\alpha$ intensity or 1.6μ surface brightness appearing almost equal. (The correlations between the $350/500 \mu$ ratio and either $H\alpha$ intensity or 1.6μ surface brightness appear almost equally correlated probably because of the noisiness of the ratio.) The difference in the correlation coefficients for the relations between the $250/350 \mu$ ratio and either 1.6μ or $H\alpha$ emission would not by

itself necessarily indicate that the total stellar population is a significantly stronger source of heating the dust at these wavelengths. However, the similarities in these correlation coefficients may be the consequence of the high scatter at low surface brightness levels in the data. An examination of the regions with the highest surface brightnesses show that the $250/350 \mu$ ratios are more strongly related to the 1.6μ surface brightnesses. The $250/350 \mu$ ratios for the binned data in Figure 8 fall within 2σ of the best fitting relation with the 1.6μ surface brightness for the regions where $I_\nu(1.6 \mu) > 10^{-5} \text{ Jy arcsec}^{-2}$. In contrast, the $250/350 \mu$ ratios for data with the highest $H\alpha$ intensities (where $I(H\alpha) > 10^{-16} \text{ erg cm}^{-2} \text{ s}^{-1} \text{ arcsec}^{-2}$) in Figure 11 frequently fall $> 3\sigma$ away from the best fit line. This variation in the dispersion can also be seen

Table 7. Results from fits between surface brightness ratios and H α intensities.

Galaxy	Surface Brightness Ratio	Slope ^a	Correlation Coefficient ^a
M81 ^b	70/160 μm	0.178 ± 0.005	0.52
	160/250 μm	0.088 ± 0.006	0.45
	250/350 μm	0.037 ± 0.007	0.33
	350/500 μm	0.039 ± 0.010	0.33
M83	70/160 μm	0.3219 ± 0.0006	0.89
	160/250 μm	0.1174 ± 0.0005	0.87
	250/350 μm	0.0352 ± 0.0006	0.77
	350/500 μm	0.0425 ± 0.0011	0.50
NGC 2403	70/160 μm	0.144 ± 0.002	0.51
	160/250 μm	0.147 ± 0.003	0.86
	250/350 μm	0.064 ± 0.002	0.78
	350/500 μm	0.051 ± 0.003	0.74

^a These quantities are for the relations describing the logarithm of the surface brightness ratios as a function of the logarithm of the H α intensity in $\text{erg cm}^{-2} \text{s}^{-1} \text{arcsec}^{-2}$.

^b Data from the inner central 5.7×3.0 arcmin (approximately the central 3 kpc) of M81 are not included in the analysis, as it primarily includes incompletely-subtracted continuum emission from the bulge.

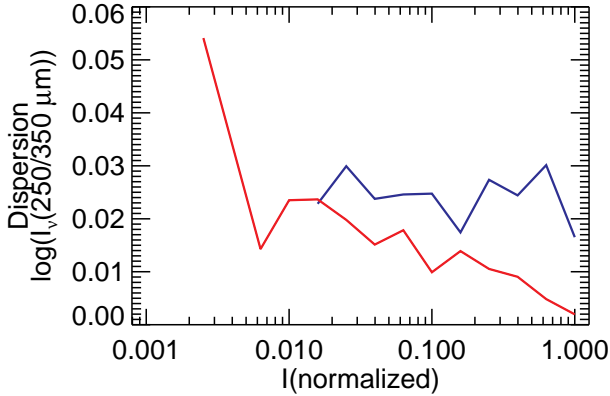


Figure 12. The weighted standard deviation of the 250/350 μm surface brightness ratio for the 36 arcsec square subregions in NGC 2403 plotted as a function of the H α intensity (blue) and 1.6 μm surface brightness (red). These curves are the same values used to plot the weighted standard deviations in Figures 8 and 11. The H α intensity and 1.6 μm surface brightness have been normalised by the value of the highest surface brightness interval.

in Figure 12, which shows the dispersion in the 250/350 μm ratio as a function of either the H α or 1.6 μm emission (after normalising both to the peak surface brightness). Additionally, the qualitative similarities between the $T_C(250/350 \mu\text{m})$ and 1.6 μm maps and the notable differences between the $T_C(250/350 \mu\text{m})$ and H α maps in Figure 7 indicate that the total stellar population is more important than star forming regions for heating the dust observed at $> 250 \mu\text{m}$. While such a result may not be surprising for M81, where the bulge is very large compared to the disc, this is particularly surprising for NGC 2403, which is a relatively bulgeless late-type spiral galaxy with widespread star formation in its disc, and we anticipate that these results may apply to other late-type spiral galaxies as well.

Table 8. Results from fits between infrared surface brightnesses and H α intensities.

Galaxy	Infrared Surface Brightness	Slope ^a	Correlation Coefficient ^a
M81 ^b	70 μm	0.834 ± 0.005	0.80
	160 μm	0.660 ± 0.005	0.74
	250 μm	0.523 ± 0.006	0.78
	350 μm	0.485 ± 0.006	0.79
	500 μm	0.433 ± 0.009	0.78
M83	70 μm	0.95 ± 0.03	0.93
	160 μm	0.66 ± 0.02	0.92
	250 μm	0.8018 ± 0.0006	0.90
	350 μm	0.7608 ± 0.0017	0.89
	500 μm	0.7153 ± 0.0012	0.90
NGC 2403	70 μm	0.7474 ± 0.0012	0.91
	160 μm	0.600 ± 0.003	0.88
	250 μm	0.511 ± 0.002	0.86
	350 μm	0.447 ± 0.002	0.86
	500 μm	0.394 ± 0.003	0.86

^a These quantities are for the relations describing the logarithm of the surface brightnesses in Jy arcsec^{-2} as a function of the logarithm of the H α intensity in $\text{erg cm}^{-2} \text{s}^{-1} \text{arcsec}^{-2}$.

^b Data from the inner central 5.7×3.0 arcmin (approximately the central 3 kpc) of M81 are not included in the analysis, as it primarily includes incompletely-subtracted continuum emission from the bulge.

We also used our binned data to compare surface brightnesses from individual far-infrared bands to H α emission so as to attempt to replicate the relations between star formation tracers and 100, 160, or 250 μm emission in M33 reported by Boquien et al. (2010) and Verlet et al. (2010). Figure 13 shows the result of this comparison, and Table 8 shows the slopes and correlation coefficients for these relations. The correlations are notably strong. In all cases, the correlation coefficients are above 0.7, which indicates that at least $> 50\%$ of the variance in the emission in any of these infrared bands can be accounted for by the relation with H α emission. These strong correlations are even seen in the relations between H α intensity and 500 μm surface brightness. However, paired with the results on how the surface brightness ratios vary with 1.6 μm surface brightness and H α intensity, it is clear that the relations seen in Figure 13 are not necessarily a consequence of the dust being directly heated by the star forming regions. Instead, the relations shown in Figure 13 may arise as a result of the dust being located in the same regions as the star forming regions. We discuss the further implications of the relations between infrared surface brightness and H α intensities in the next section.

4.4 Relative contributions of total stellar populations and star formation to dust heating

In prior sections, we performed comparisons between surface brightness ratios and the emission from either the total stellar populations or star forming regions. When the surface brightness ratio variations are much more strongly correlated with one source of dust heating than with the other, we can draw very sharp conclusions about the dust heating. For example, we can confidently conclude that the 70/160 μm surface brightness ratio variations in NGC 2403 are primarily dependent on heating by star forming regions, while we can also say that the 250/350 μm variations in M81 are dependent on heating by the total stellar population. How-

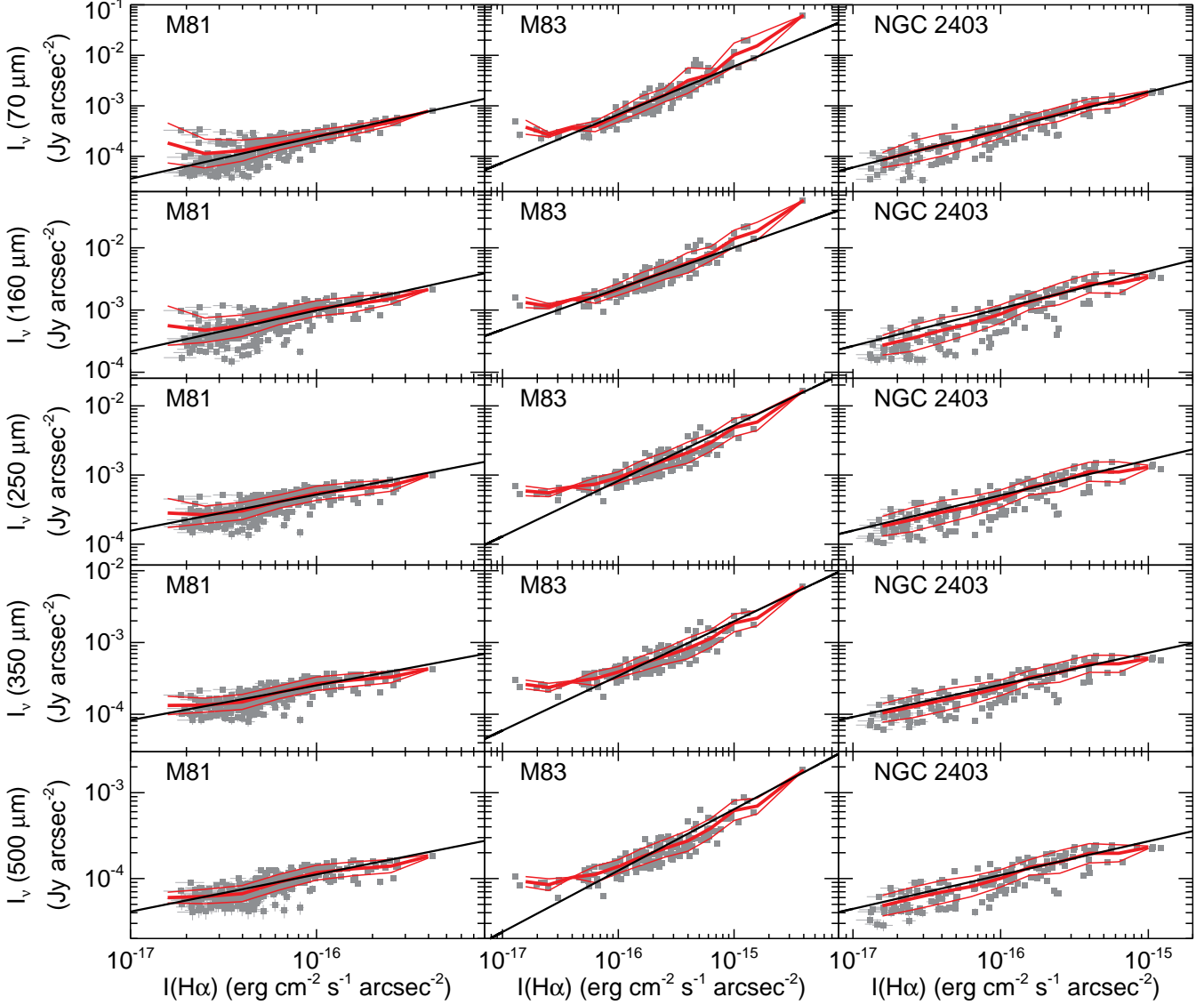


Figure 13. Comparisons of infrared surface brightnesses in individual wave bands to the $H\alpha$ intensities for the 36 arcsec square subregions in the sample galaxies. The solid lines show the best fit lines. The thick red line shows the weighted mean of the ratios averaged over intervals with a width of 0.2 in $\log(I(H\alpha))$, and the thinner red lines show the weighted standard deviation of the data (except when one data point falls within an interval, in which case the uncertainty in the data point is used). Data from the inner central 5.7×3.0 arcmin (approximately the central 3 kpc) of M81 are not included in the analysis, as it primarily includes incompletely-subtracted continuum emission from the bulge. Parameters related to the fits are shown in Table 8.

ever, the above comparisons have not been as effective in revealing which dust heating source is dominant in cases where the correlations produce similar correlation coefficients, as, for example, in the case of the 160/250 μm data for NGC 2403.

To address this issue, we attempt to fit the surface brightness ratios for the 36 arcsec square subregions as a function of both 1.6 μm and $H\alpha$ emission. The equation we fit to the data is based on

$$CT^{4+\beta} = E_{IN}, \quad (6)$$

a generalised version of the Stefan-Boltzmann law for the case of blackbody emission modified by an emissivity function described by a power law with a coefficient β . E_{IN} will be equal to the total

energy from all dust heating sources and can be written as the sum of scaled versions of the 1.6 μm and $H\alpha$ emission. For a small range in temperature variation (as is the case for our data), T can be related to a surface brightness ratio through a power law. The difference between the actual colour temperatures and the colour temperatures from this power law differ by only $\sim 2\%$ over the range of surface brightness ratios that we are using; this is usually lower than the uncertainties in the ratios themselves. Given this, we can represent Equation 6 as

$$C_1 \left(\frac{I_\nu(\lambda_1)}{I_\nu(\lambda_2)} \right)^{\frac{1}{\alpha}} = C_2 I(H\alpha) + C_3 I_\nu(1.6\mu\text{m}), \quad (7)$$

or we can rewrite this in logarithmic form as

$$\ln \left(\frac{I_\nu(\lambda_1)}{I_\nu(\lambda_2)} \right) = \alpha \ln(C_2 I(\text{H}\alpha) + C_3 I_\nu(1.6\mu\text{m})) - \ln(C_1). \quad (8)$$

Equation 8 can be simplified as

$$\ln \left(\frac{I_\nu(\lambda_1)}{I_\nu(\lambda_2)} \right) = \alpha \ln(I(\text{H}\alpha) + A_1 I_\nu(1.6\mu\text{m})) + A_2. \quad (9)$$

Equation 9 can be thought of as similar to the relations typically shown between colour and flux or variants of these quantities (such as Figures 8 and 11) but with two flux quantities simultaneously fit to the colour instead of one. The relative contribution of star forming regions to the dust heating can be calculated using

$$\frac{E_{SF}}{E_{Total}} = \frac{I(\text{H}\alpha)}{I(\text{H}\alpha) + A_1 I_\nu(1.6\mu\text{m})}. \quad (10)$$

This approach to determining the relative contributions of star forming regions and the total stellar population to dust heating is relatively simplistic. More complex models would be able to more accurately describe the propagation of photons through the ISM, the absorption of light by dust, the range of dust temperatures, and the dust emission, but this requires making many assumptions about the stellar populations and the physical properties of the dust particles. In contrast, the analysis we have outlined above relies primarily upon the assumptions that dust heating occurs locally and that the relation between surface brightness ratios and temperatures follow power laws. Hence, it can be used as a way to examine dust heating from two energy sources using measurements that are independent of dust surface density in a way that relies upon very few assumptions.

We fit Equation 8 to the 36 arcsec square subregions in each galaxy, as it was easier to use this equation with a Levenberg-Marquardt algorithm to converge upon the best fit to the data, even though the solution is degenerate. We then used these results to calculate the parameters for Equation 9. Table 9 given the best fitting parameters along with the correlation coefficients for the values given by the right and left sides of Equation 9 and the fractional contribution of star forming regions to dust heating as given by Equation 10. Uncertainties in the quantities in Table 9 are calculated using a monte carlo approach in which we perform fits in a series of iterations by adding Gaussian noise to the data and then measure the standard deviation in the results. Figure 14 shows the relations between the surface brightness ratios and the best fitting relations. Additionally, we used these results along with Equation 5 to create colour temperature maps constructed from the $\text{H}\alpha$ and $1.6\mu\text{m}$ images. These reconstructed colour temperature maps as well as the colour temperature maps based on the observed surface brightness ratios and maps of the relative contribution of star forming regions to dust heating are all shown in Figures 15-17.

We encountered two problems with fitting Equation 8 to the data. In fitting the $70/160\mu\text{m}$ surface brightness data for M83, we found that the difference between the ratio and the resulting fit was significantly high around the nucleus, and the reconstructed colour temperature map in Figure 16 did not look like the observed colour temperature map. Additionally, the fractional contribution of star formation to dust heating seemed abnormally low; when the nucleus is included, the fractional contribution of star formation to dust heating is ~ 0.3 . This implies that the nucleus does not follow the same $70/160\mu\text{m}$ dust heating relation as the rest of the disc, for reasons that are unclear but that could be related to hot ($\sim 100\text{ K}$) dust heated by the nuclear starburst that is visible in the $70\mu\text{m}$ band. Therefore, we excluded the central 3×3 regions

(108×108 arcsec) of M83 for the analysis on the $70/160\mu\text{m}$ ratio. (Excluding the same central region when fitting Equation 8 to the $160/250$, $250/350$, or $350/500\mu\text{m}$ data did not affect the fits significantly.) In fitting Equation 8 to the $70/160\mu\text{m}$ data for NGC 2403, we found that the $C_3 I_\nu(1.6\mu\text{m})$ term was negligible compared to the $C_2 I(\text{H}\alpha)$ term, which caused convergence problems when trying to perform a nonlinear least squares fit. We therefore report results in which the $70/160\mu\text{m}$ ratio is a function of only the $\text{H}\alpha$ intensities (which is consistent with the interpretation that variations in dust heating traced by this ratio depend primarily on star formation).

After dealing with these two exceptions, the resulting fits are generally very good. The correlation coefficients in Table 9 for the relations between the logarithm of the surface brightness ratios and the expression on the right side of Equation 9 are generally higher than the corresponding correlation coefficients in either Tables 4 or 7 for fits to either the $1.6\mu\text{m}$ or $\text{H}\alpha$ emission, although in many cases, the improvement in the correlation coefficients is marginal. Moreover, most correlation coefficients in Table 9 are above 0.7, indicating that at least 50% of the variance in the data can be accounted for by the relations. The only exceptions are the $70/160\mu\text{m}$ ratio for NGC 2403, which we identified as problematic up above, and the $350/500\mu\text{m}$ ratio for M83, which is very noisy in general.

The reconstructed colour temperature maps based on Equation 9 in Figures 15-17 look qualitatively similar to the colour temperature maps based on the observed surface brightness ratios. The reconstructed maps generally match the overall radial gradients in temperature seen in many of the observed maps, and the reconstructed maps also show that we could reproduce the colour temperatures of many of the individual star forming regions within the spiral structures of each galaxy. However, the temperatures of the reconstructed star forming regions do not always precisely match the colour temperatures in the observed map. This could be because of variable extinction among individual star forming regions, which could cause the relation between star formation (as traced by $\text{H}\alpha$ emission) and dust heating to vary. We also occasionally see some residual structures in temperature that show features that are not quite described by the reconstructed map. In M81, the nucleus (excluded from the fits) appears notably cold in the residual maps because of the synchrotron emission from the AGN. The nucleus of M83, which caused problems in the fits and was excluded, appears as a hot spot in the residual $70/160\mu\text{m}$ map. Residual spiral structure is seen in the $160/250\mu\text{m}$ and $250/350\mu\text{m}$ residual maps, which could be indicative of dust heating gradients across the spiral arms that are inadequately described by Equation 9 and show the limitations of using this approach to reproducing dust colour temperature variations. Foyle et al. (in preparation) found a similar offset between dust temperatures and star formation in the spiral arms. Finally, we see residual structure in the $70/160\mu\text{m}$ map of NGC 2403 that is clearly a result of latent image effects in the $70\mu\text{m}$ data.

The main purpose of these fits was to determine the relative contributions of star forming regions and the total stellar populations to dust heating. The results in Table 9 generally show a decrease in the relative contribution of dust heating from star formation as wavelength increases. In M83 and NGC 2403, star forming regions contribute $> 50\%$ of the total heating of the dust traced by the $< 250\mu\text{m}$ bands, although in M81, the dust heating up to $70\mu\text{m}$ appears to still be dominated by the total stellar population. At longer wavelengths, the relative contribution of star forming regions decreases significantly. Star forming regions appear to contribute only $< 30\%$ of the energy for heating the dust traced by

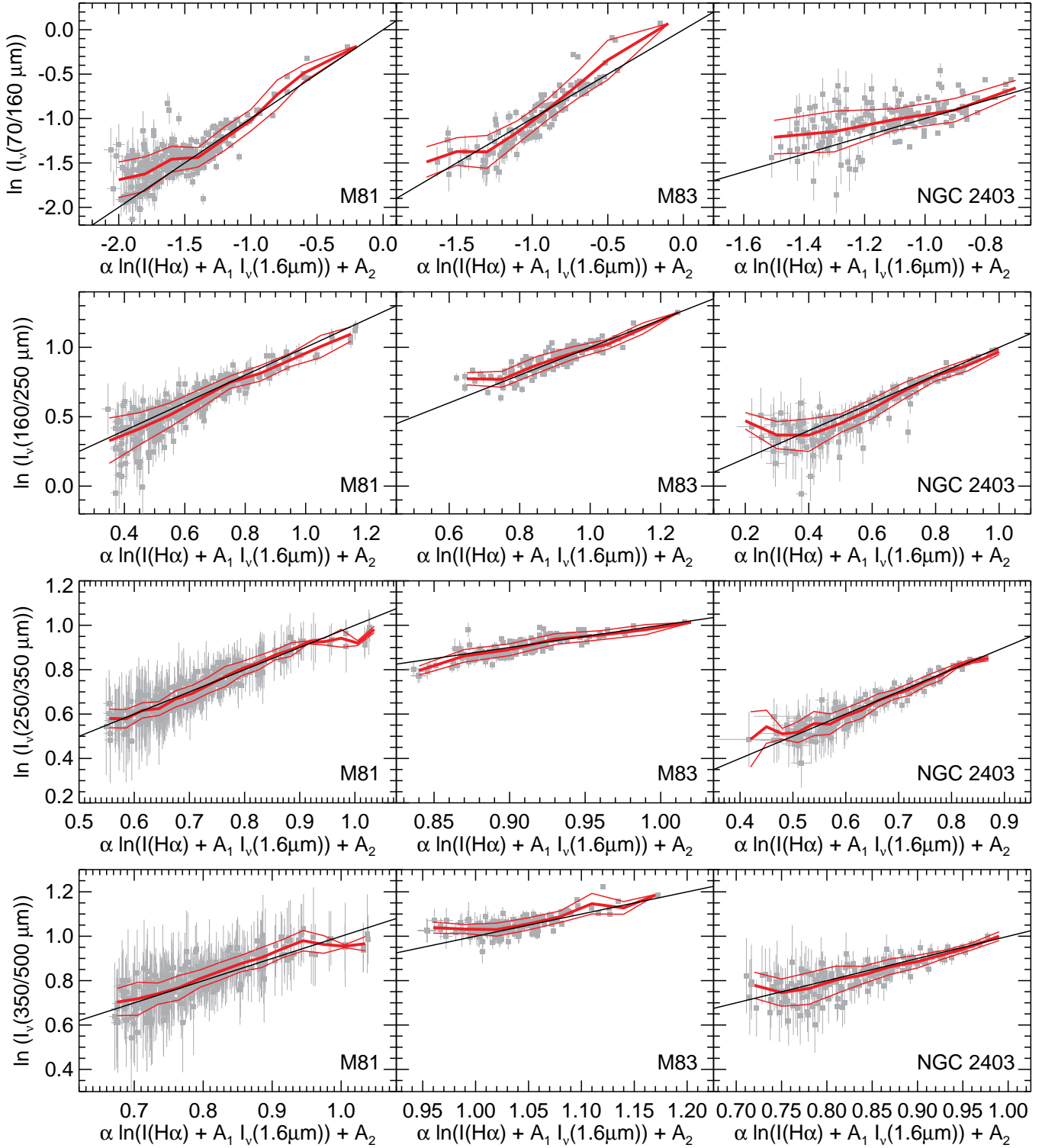


Figure 14. Comparisons of the surface brightness ratios to the relation described by Equation 9 for the 36 arcsec square subregions in the sample galaxies. The solid lines show the best fit lines, which have a slope of 1. The thick red line shows the weighted mean of the ratios averaged over different interval widths for each surface brightness ratio (0.2 in the units of the x-axes for the 70/160 μm ratio, 0.1 for the 160 μm ratio, and 0.03 for the 250/350 μm and 350/500 μm ratios), and the thinner red lines show the weighted standard deviation of the data (except when one data point falls within an interval, in which case the uncertainty in the data point is used). Data from the inner central 3×3 subregions (108×108 arcsec) of M83 are not included in the analysis, as it caused problems during the fit as described in the text. Parameters related to the fits are shown in Table 9.

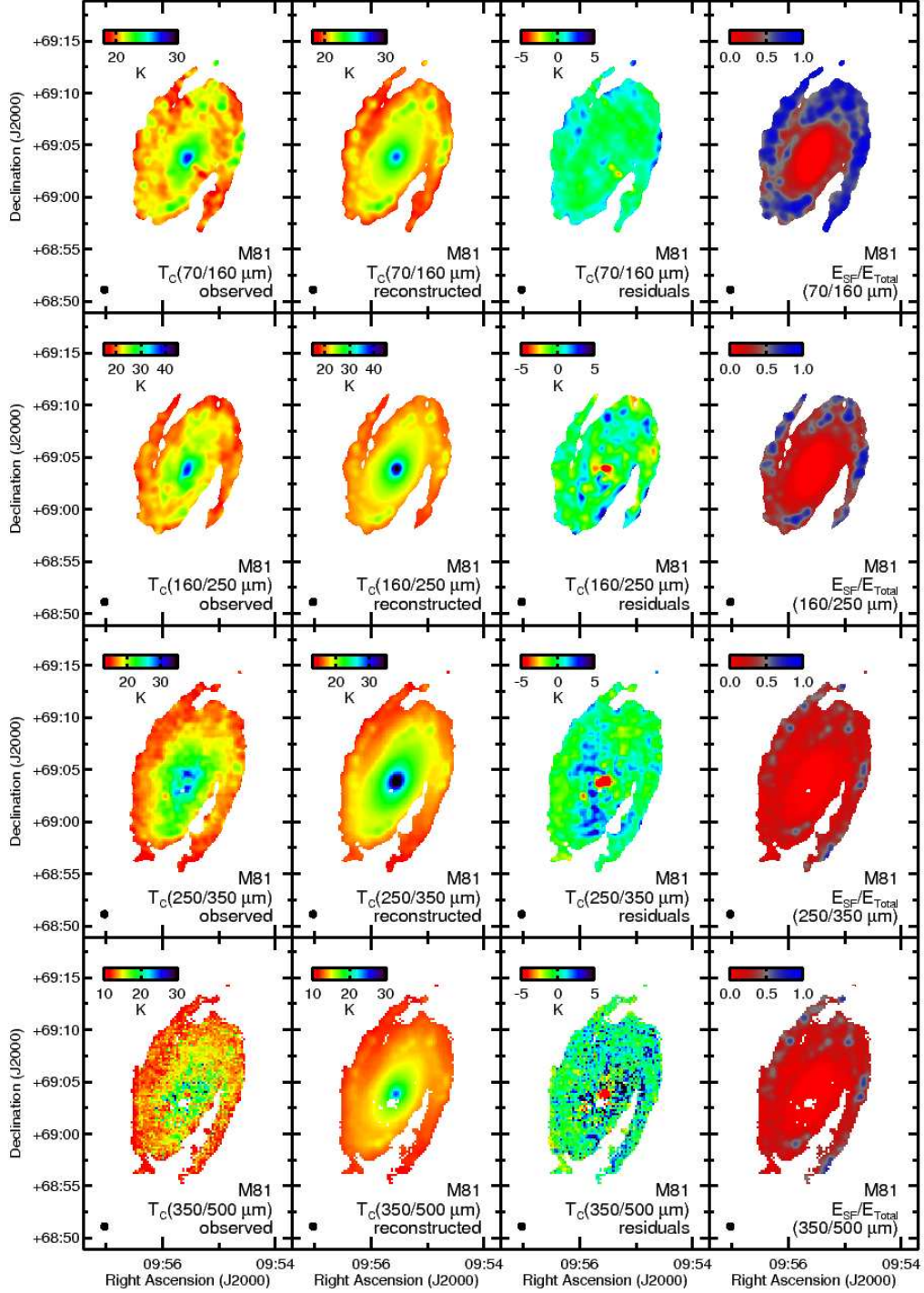


Figure 15. The left column shows the observed colour temperature maps of M81. The next column shows the colour temperature maps reconstructed using Equation 5 and 9, the $\text{H}\alpha$ and $1.6 \mu\text{m}$ images, and the parameters in Table 9. The third column shows the residual values when the reconstructed image is subtracted from the observed image. The fourth column shows the fraction of dust heating that is attributed to star formation as traced by the given surface brightness ratio; these images are created using Equation 10, the $\text{H}\alpha$ and $1.6 \mu\text{m}$ images, and the A_1 parameters in Table 9. All of these maps were created from data where the PSF was matched to the PSF of the $500 \mu\text{m}$ data, which has a FWHM of 36 arcsec (shown by the black circles in the lower left corner of each panel). This 36 arcsec circle is also the same width as the bins used in the analysis in Sections 4.2 and 4.3. Pixels where the signal was not detected at the 5σ level in both bands used to create the observed colour temperature maps were left blank (white). In the other three columns, these pixels are left blank and pixels where data are not detected at the 5σ level in either the $\text{H}\alpha$ or $1.6 \mu\text{m}$ images were left blank. Each map is 30×20 arcmin, and north is up and east is left in each panel.

Table 9. Results from fitting surface brightness ratios as a function of both H α and 1.6 μ m emission.

Galaxy	Surface Brightness Ratio	A_1^{ab}	A_2^a	α^a	E_{SF}/E_{Total}^c	Correlation Coefficient ^d
M81	70/160 μ m	$(2.25 \pm 0.05) \times 10^{-12}$	12.01 ± 0.12	0.369 ± 0.004	0.361 ± 0.006	0.76
	160/250 μ m	$(5.4 \pm 0.6) \times 10^{-12}$	7.3 ± 0.2	0.185 ± 0.005	0.19 ± 0.02	0.89
	250/350 μ m	$(1.3 \pm 0.4) \times 10^{-11}$	4.3 ± 0.2	0.100 ± 0.006	0.09 ± 0.03	0.93
	350/500 μ m	$(1.2 \pm 1.1) \times 10^{-11}$	3.6 ± 0.3	0.078 ± 0.007	0.10 ± 0.06	0.82
M83	70/160 μ m	$(5.7 \pm 1.2) \times 10^{-13e}$	8.91 ± 0.12^e	0.274 ± 0.004^e	0.924 ± 0.014^e	0.89^e
	160/250 μ m	$(1.06 \pm 0.08) \times 10^{-12}$	5.21 ± 0.02	0.120 ± 0.001	0.854 ± 0.009	0.88
	250/350 μ m	$(1.02 \pm 0.17) \times 10^{-11}$	2.24 ± 0.03	0.038 ± 0.001	0.38 ± 0.04	0.85
	350/500 μ m	$(1 \pm 3) \times 10^{-10}$	2.63 ± 0.06	0.048 ± 0.001	0.06 ± 0.04	0.66
NGC 2403	70/160 μ m	0^f	4.23 ± 0.02^f	0.144 ± 0.002^f	1^f	0.51^f
	160/250 μ m	$(6.2 \pm 0.6) \times 10^{-12}$	6.39 ± 0.10	0.158 ± 0.003	0.65 ± 0.02	0.89
	250/350 μ m	$(1.1 \pm 0.3) \times 10^{-10}$	3.32 ± 0.09	0.077 ± 0.002	0.10 ± 0.03	0.93
	350/500 μ m	$(1.6 \pm 0.6) \times 10^{-11}$	2.83 ± 0.13	0.055 ± 0.002	0.42 ± 0.08	0.76

^a These parameters correspond to the ones in Equation 9.^b The units of A_1 are $(\text{erg cm}^{-2} \text{s}^{-1} \text{arcsec}^{-2}) (\text{MJy sr}^{-1})^{-1}$.^c This is relative fraction of dust heating from star forming regions as given by Equation 10. The value is calculated with the data for all 36 arcsec square regions used when fitting Equation 9 to the data.^d These are correlation coefficients for the relations between the right and left sides of Equation 9.^e These fits were performed excluding the central 3×3 36 arcsec square regions. See the text for details.^f Instead of reporting the result from the fit to Equation 8 here, we instead report the result of the fit of a power law relation between the 70/160 μ m surface brightness ratio and the H α intensity. See the text for details.

the 250/350 μ m and 350/500 μ m bands in all three galaxies. The relation for the 350/500 μ m ratio for NGC 2403 seems anomalous in that it implies that $\sim 40\%$ of the energy for the dust heating originates from star forming regions, which is higher than what is implied by the fit to the 250/350 μ m ratio for that galaxy. However, we suspect that this is because the 350/500 μ m data are on the Rayleigh-Jeans side of the SED and are strongly affected by noise. Hence, colour variations related to dust heating are not detected at a high signal-to-noise level in NGC 2403, and so the methods we are using may not be effective in this one case.

Overall, the results here are consistent with the interpretations we have provided for the results in Sections 4.2 and 4.3. At wavelengths shorter than 160 μ m, most of the dust appears to be heated by star forming regions in these galaxies, which is why the 70/160 μ m ratios appear more closely dependent on the H α surface brightnesses. At wavelengths longer than 250 μ m, the dust appears to be primarily heated by the total stellar populations, and so the 250/350 μ m and 350/500 μ m ratios are more strongly related to the 1.6 μ m surface brightness.

5 DISCUSSION

The results here have demonstrated that the total stellar population, including evolved stars and not just stars in star forming regions, plays a significant role in heating dust in nearby galaxies. The fraction of observed dust emission that is heated by the total stellar population varies as a function of the wavelength. While star forming regions are the dominant heating source for dust observed at < 160 μ m, the total stellar population, including evolved stars, become the dominant heating source for the dust observed at > 250 μ m. We have been able to demonstrate that dust is heated by the total stellar populations in spite of the fact that the dust emission itself tends to be correlated with H α emission, which should bias our results towards finding dust heated by star formation. More-

over, we have shown that significant dust heating by the total stellar population can be seen even in late-type spiral galaxies.

The results here validate the original conclusions drawn from IRAS data by Lonsdale Persson & Helou (1987), Walterbos & Schwing (1987), Sauvage & Thuan (1992), Walterbos & Greenawalt (1996), and Kong et al. (2004) as well as the conclusions drawn from *Spitzer* data by Hinz et al. (2004) and Calzetti et al. (2010) that evolved stellar populations play an increasingly important role in heating dust towards longer infrared wavelengths. Additionally, the differences between the results for M81, where we were able to demonstrate that the bulge stars were heating dust even at 70 μ m, and the results for NGC 2403, where the dust emitting at 70 μ m did not appear to be influenced at all by the bulge stars, corroborates results from Engelbracht et al. (2010), who found that bulges influenced dust heating in nearby galaxies.

Furthermore, the results here corroborate the findings from radiative transfer models (e.g. da Cunha et al. 2008; Bianchi 2008; Popescu et al. 2011) as well as other dust emission models (e.g. Draine et al. 2007) that had suggested that dust absorption and emission can only be accurately modelled if it contains a dust component heated by star formation and a dust component heated by the total stellar population. Both our results and the radiative transfer analyses suggest that the < 160 μ m emission originates from dust that is heated by star forming regions located within clouds (or clumps) that are optically thick at ultraviolet and blue wavelengths. In these models, only a relatively small fraction of the dust is heated by the star forming regions, but the dust appears significantly brighter than the dust outside the centres of the regions, leading to higher 70/160 μ m surface brightness ratios in these regions. Most of the dust mass in the ISM, however, is shielded from the ultraviolet and blue photons from the star forming regions. This dust is heated by the diffuse interstellar radiation field, which would include light from evolved stars, and has lower temperatures. None the less, because a much greater fraction of the dust mass is heated this way, the colder dust is the predominant source of emission at > 250 μ m. Also, if the mean free path of light in the diffuse inter-

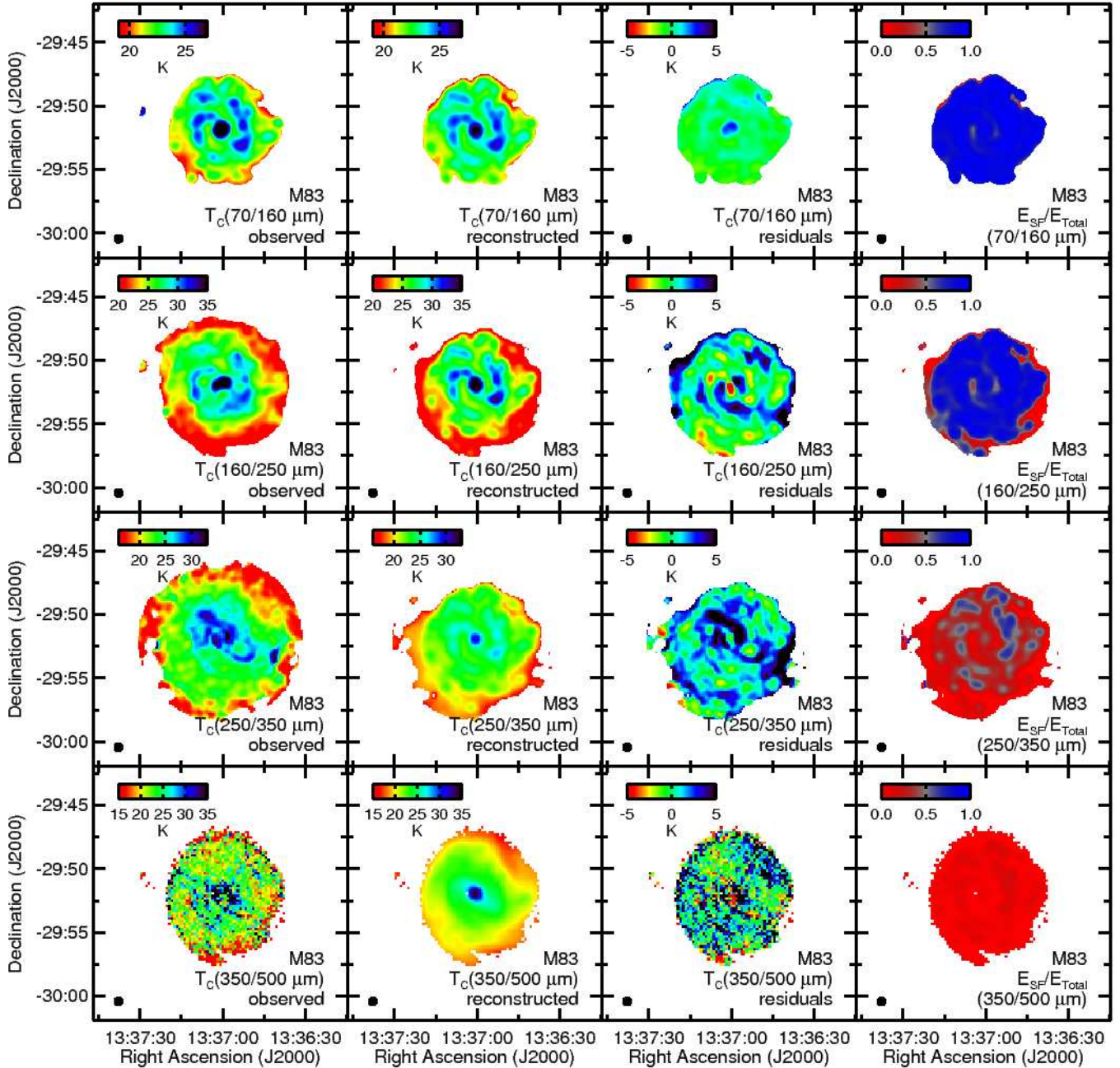


Figure 16. The observed and reconstructed colour maps for M83, the residual values when the reconstructed maps are subtracted from the observed maps, and the E_{SF}/E_{Total} maps. Each map is 20×20 arcmin. See the caption of Figure 15 for other information about the layout.

stellar medium is similar to or smaller than the resolution elements in our analysis, the 250/350 μm and 350/500 μm ratios can be expected to be very well correlated with the stellar surface brightnesses in those resolution elements. The V-band optical depths and the dust vertical scale heights derived in the analyses of edge-on galaxies by Xilouris et al. (1999) and Bianchi (2007) imply that the mean free paths of V-band photons through the discs of spiral galaxies should be roughly between 0.1 and 1 kpc. In comparison, the binned data that we used correspond to physical sizes of ~ 500 -

800 pc, and so the 250/350 μm and 350/500 μm ratios should be very well correlated with tracers of the total stellar population in these binned data, which is exactly what we see.

While we do produce observational results that are generally consistent with many previously-published dust models, we do find an inconsistency when comparing our results for M81 and NGC 2403 with the dust models for these specific galaxies from Draine et al. (2007). Draine et al. (2007) did predict from their SED fitting to M81 that most of the dust emission at $> 70 \mu\text{m}$ is from

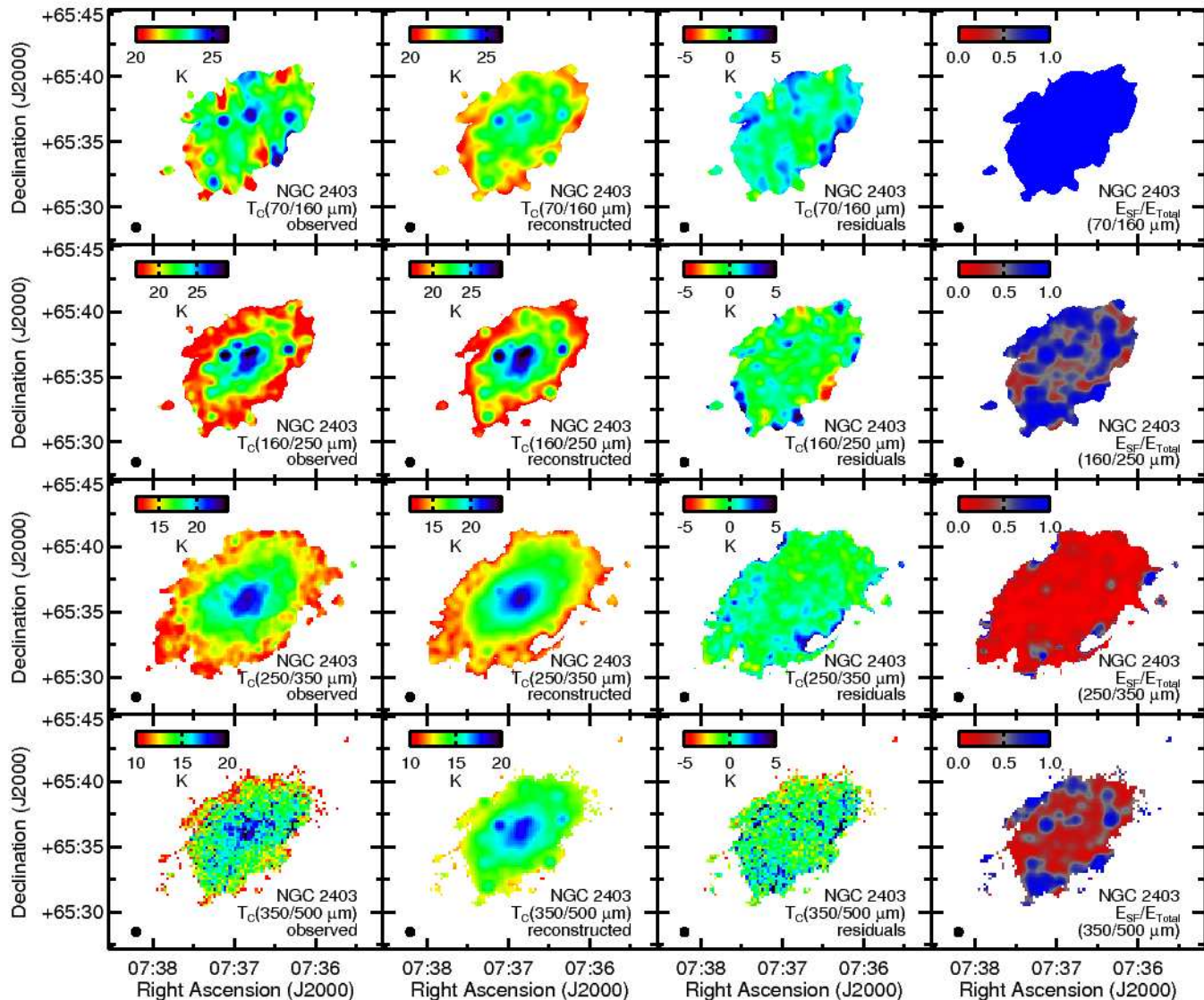


Figure 17. The observed and reconstructed colour maps for NGC 2403, the residual values when the reconstructed maps are subtracted from the observed maps, and the E_{SF}/E_{Total} maps. Each map is 21×18 arcmin. See the caption of Figure 15 for other information about the layout.

a diffuse component, which is largely consistent with the results from our surface brightness ratio variations. However, their SED fitting to NGC 2403 also predicted that most of the dust emission at $> 70 \mu\text{m}$ from that galaxy was from diffuse dust, whereas the surface brightness variations we observed imply that the star forming regions should be the predominant heating source at $< 160 \mu\text{m}$. This demonstrates that, while the general ideas being applied in dust models are still valid, further refinement is needed if the models are not only going to replicate the overall SEDs of galaxies but also replicate colour variations within the galaxies.

Even though many authors have argued that a significant fraction of the dust in nearby spiral galaxies is heated by evolved stellar populations, other authors have shown that total infrared dust emission can be correlated with star formation in nearby spiral galaxies (Devereux & Young 1990; Devereux et al. 1995; Buat & Xu 1996;

Kennicutt et al. 2009), and even some of the early results from *Herschel* suggest that emission in individual wave bands (i.e. the 100, 160, and $250 \mu\text{m}$ bands) can be correlated with other star formation tracers in M33 (Boquien et al. 2010; Verlet et al. 2010), a galaxy with the same Hubble type as NGC 2403. We think the apparent contradictions between the correlations between far-infrared emission and star formation found by other authors and the relation between dust heating and the total stellar populations that we find can be explained in two ways.

First of all, some of the correlations between far-infrared emission and star formation are based on either the far-infrared fluxes traced by the IRAS 60– $100 \mu\text{m}$ data or on the total dust emission as computed from the *Spitzer* 24– $160 \mu\text{m}$ bands, both of which strongly sample emission from dust on the Wien side of the thermal dust emission in a regime where we also found that star forma-

tion strongly influenced dust heating. Moreover, IRAS-based studies simply did not have data at $>100\ \mu\text{m}$ wavelengths, which we found were dominated by emission from dust heated by the total stellar population.

Second, it is possible that far-infrared emission could be linked to star formation indirectly through the Schmidt law (Schmidt 1959; Kennicutt 1998b) rather than directly through dust heating. Dust emission at far-infrared wavelengths is a function of both dust temperature and dust surface density. Since dust should implicitly be a tracer of the total surface density of gas in the interstellar medium, and since the Schmidt law suggests that star formation is a function of the amount of gas available to fuel it, we expect dust emission to be correlated with star formation to some degree even if the dust is not directly heated by the star formation. The dust colours, however, are strongly affected by dust temperature but are independent of dust surface density and therefore will depend more on dust heating sources than the emission observed in a single wave band. This is probably why we are able to show that far-infrared surface brightness in the $250\text{--}500\ \mu\text{m}$ bands is correlated with $\text{H}\alpha$ intensity even though we have demonstrated that the $250/350\ \mu\text{m}$ and $350/500\ \mu\text{m}$ surface brightness ratios are more strongly correlated with $1.6\ \mu\text{m}$ surface brightness. Additionally, in the case of M81, the $1.6\ \mu\text{m}$ emission is poorly correlated with the 250 , 350 , and $500\ \mu\text{m}$ surface brightness, and yet the $250/350\ \mu\text{m}$ and $350/500\ \mu\text{m}$ ratios are clearly being heated mostly by the stellar population traced by the $1.6\ \mu\text{m}$ band. In this case the infrared surface brightness can only be correlated with the $\text{H}\alpha$ emission if the dust surface density is correlated with the star formation surface density. We believe that this may also be a possible reason why Boquien et al. (2010) and Verlet et al. (2010) can show that the $100\text{--}250\ \mu\text{m}$ emission is correlated with $\text{H}\alpha$ and $24\ \mu\text{m}$ emission, although a comparison of the infrared colour variations in M33 to tracers of star formation or the total stellar population would be needed to confirm this.

Aside from the use of surface brightness ratios instead of surface brightnesses or flux densities in our analysis, we think that the choice of galaxies that we used in this analysis was critical to demonstrating that the total stellar populations (including evolved stars) play a significant role in dust heating. M81 and NGC 2403 are both special in that the stellar emission traces different structures than either the dust emission or the star formation. This has been critically important for allowing us to disentangle the relative contributions from the two different heating sources. M83 is a good example of a “typical” spiral galaxy in which the starlight, dust emission, and star formation all trace similar structures. Our analysis demonstrates that it is difficult to disentangle whether the total stellar population or star formation is a greater contributor to dust heating in such cases. Other authors working with M83 or similar galaxies will probably encounter similar problems.

We emphasize that we have only found that these results apply to spiral galaxies. Galametz et al. (2010) demonstrated that the $250/500\ \mu\text{m}$ surface brightness ratio depends on $24\ \mu\text{m}$ surface brightness in the dwarf irregular galaxy NGC 6822, thus demonstrating that the dust emitting at submillimetre wavelengths was significantly affected by star forming regions. This is probably a result of the galaxy containing relatively few evolved stars that could heat dust, although it is conceivable that, in the low metallicity environment, the interstellar medium would contain less dust, and so diffuse dust would be less shielded from star forming regions. We anticipate that similar results would be obtained for other dwarf irregular galaxies with ongoing star formation. In contrast, we may expect that the $>70\ \mu\text{m}$ emission seen in elliptical galaxies (when

the elliptical galaxies produce any far-infrared emission at all) will originate from dust predominantly heated by evolved stars, just as the dust from the central 3 kpc of M81 appears to be heated primarily by evolved stars. How our results for spiral galaxies apply to luminous infrared galaxies (with total infrared luminosities between 10^{11} and $10^{12}\ L_{\odot}$) and ultraluminous galaxies (with total infrared luminosities above $10^{12}\ L_{\odot}$) is unclear, as the galaxies contain strong star formation and AGN emission but also have large stellar populations and may have large reservoirs of dust that is shielded from the star forming and AGN regions. Additional analyses on the dust heating mechanisms in these classes of galaxies is warranted.

6 CONCLUSIONS

For M81, M83, and NGC 2403, we have demonstrated that the $250/350\ \mu\text{m}$ and $350/500\ \mu\text{m}$ surface brightness ratios are more strongly correlated with $1.6\ \mu\text{m}$ emission, which traces the starlight from the total stellar populations including evolved stars, than with $\text{H}\alpha$ emission from star-forming regions. At shorter wavelengths, the total stellar population may continue to be influential in dust heating, particularly in early-type spiral galaxy M81, but heating by star formation becomes more important, particularly in the late-type spiral galaxy NGC 2403. None the less, these results imply that, in each of these galaxies as well as other spiral galaxies in general, the total stellar populations are a significant if not dominant heating source for the dust observed at $>160\ \mu\text{m}$ in all spiral galaxies, including late-type spiral galaxies. In some cases, virtually all of the emission may originate from dust heated by the total stellar populations, including evolved stars in the bulges and discs.

The results here have strong implications for modeling dust in spiral galaxies. First of all, dust models need to include separate thermal components for the dust heated by star forming regions and dust heated by the total stellar populations. When fitting single modified blackbodies to data, it may be inappropriate to force the function to fit $70\ \mu\text{m}$ or shorter wavelength data, particularly by varying the index of the power law that describes the dust emissivity (see, for example, Dunne et al. (2000), but also note the additional analysis in Dunne & Eales (2001)). Models based on more complex dust physics need to include components heated by red stellar radiation fields that only become predominant at longer wavelengths, as is already done in some cases, and these models also need to be tuned so that they replicate not only the global SEDs of galaxies but also the colour variations within galaxies. Template-based SED models need to include an additional component based on dust heated by a quiescent stellar population, as is done by Rowan-Robinson et al. (2010), although these cold dust templates should be calibrated using observations of nearby galaxies where the dust emission can be studied on kpc scales rather than inferred from observations of unresolved sources. Also, dust extinction corrections that rely upon infrared flux to estimate extinction corrections, as is commonly done for ultraviolet data (e.g. Meurer et al. 1999), need to account for dust heating by evolved stellar populations and not just star forming regions, as is also suggested by Kong et al. (2004) and Cortese et al. (2008). Finally, we are going to suggest caution when using far-infrared emission as a star formation tracer for both nearby and more distant galaxies. Dust emission in individual wave bands at $>160\ \mu\text{m}$ is probably related to star formation indirectly through the Schmidt law rather than directly through dust heating. Using, for example, $250\ \mu\text{m}$ flux density measurements to determine star formation rates is akin to

using CO measurements to determine star formation rates. While this may still be an accurate way to measure star formation rates under certain circumstances, it will be necessary to understand the caveats that affect such analyses.

ACKNOWLEDGMENTS

G.J.B. thanks Simone Bianchi and the reviewer for helpful comments on this paper. G.J.B. was funded by the STFC. The research of C.D.W. and K.F. is supported by grants to C.D.W. from the Canadian Space Agency and the Natural Sciences and Engineering Research Council of Canada. PACS has been developed by a consortium of institutes led by MPE (Germany) and including UVIE (Austria); KU Leuven, CSL, IMEC (Belgium); CEA, LAM (France); MPIA (Germany); INAF-IFSI/OAA/OAP/OAT, LENS, SISSA (Italy); IAC (Spain). This development has been supported by the funding agencies BMVIT (Austria), ESA-PRODEX (Belgium), CEA/CNES (France), DLR (Germany), ASI/INAF (Italy), and CICYT/MCYT (Spain). SPIRE has been developed by a consortium of institutes led by Cardiff University (UK) and including Univ. Lethbridge (Canada); NAOC (China); CEA, LAM (France); IFSI, Univ. Padua (Italy); IAC (Spain); Stockholm Observatory (Sweden); Imperial College London, RAL, UCL-MSSL, UKATC, Univ. Sussex (UK); and Caltech, JPL, NHSC, Univ. Colorado (USA). This development has been supported by national funding agencies: CSA (Canada); NAOC (China); CEA, CNES, CNRS (France); ASI (Italy); MCINN (Spain); SNSB (Sweden); STFC (UK); and NASA (USA). HIPE is a joint development by the Herschel Science Ground Segment Consortium, consisting of ESA, the NASA Herschel Science Center, and the HIFI, PACS and SPIRE consortia. This research has made use of the NASA/IPAC Extragalactic Database (NED) which is operated by the Jet Propulsion Laboratory, California Institute of Technology, under contract with the National Aeronautics and Space Administration.

REFERENCES

- Allen R. J., Knapen J. H., Bohlin R., Stecher T. P., 1997, *ApJ*, 487, 171
- Arendt R. G. et al., 1998, *ApJ*, 508, 74
- Bendo G. J. et al., 2007, *MNRAS*, 380, 1313
- Bendo G. J. et al., 2008, *MNRAS*, 389, 629
- Bendo G. J. et al., 2010a, *MNRAS*,
- Bendo G. J. et al., 2010b, *A&A*, 518, L65
- Bianchi S., 2007, *A&A*, 471, 765
- Bianchi S., 2008, *A&A*, 490, 461
- Bohlin R. C., Cornett R. H., Hill J. K., Smith A. M., Stecher T. P., 1983, *ApJ*, 274, L53
- Boissier S. e al., 2005, *ApJ*, 619, L83
- Boquien M. et al., 2010, *A&A*, 518, L70
- Boselli A., Gavazzi G., 2002, *A&A*, 386, 124
- Buat V., Xu C., 1996, *A&A*, 306, 61
- Calzetti D. et al., 2005, *ApJ*, 633, 871
- Calzetti D. et al., 2007, *ApJ*, 666, 870
- Calzetti D. et al., 2010, *ApJ*, 714, 1256
- Comte G., 1981, *A&AS*, 44, 441
- Condon J. J., Condon M. A., Gisler G., Puschell J. J., 1982, *ApJ*, 252, 102
- Cortese L., Boselli A., Franzetti P., Decarli R., Gavazzi G., Boissier S., Buat V., 2008, *MNRAS*, 386, 1157
- da Cunha E., Charlot S., Elbaz D., 2008, *MNRAS*, 388, 1595
- Dale D. A. et al., 2007, *ApJ*, 655, 863
- Davies J. I. et al., 2010, *MNRAS*, 409, 102
- de Blok W. J. G., Walter F., Brinks E., Trachternach C., Oh. S.-H., Kennicutt R. C., Jr, 2008, *AJ*, 136, 2648
- de Vaucouleurs G., de Vaucouleurs A., Corwin H. G., Buta R. J., Paturel G., Fouque P., 1991, *Third Reference Catalogue of Bright Galaxies*, Springer-Verlag, Berlin
- Devereux N. A., Jacoby G., Ciardullo R., 1995, *AJ*, 110, 1115
- Devereux N. A., Young J. S., 1990, *ApJ*, 350, L25
- Devereux N. A., Young J. S., 1992, *AJ*, 103, 1536
- Devereux N. A., Young J. S., 1993, *AJ*, 106, 948
- Dowell C. D. et al., 2009, in Oschmann J. M. Jr. Clampin M. C., MacEwen H. A., eds, *Proceedings of the SPIE, Space Telescopes and Instrumentation 2010: Optical, Infrared, and Millimeter Wave*. SPIE, Bellingham, p. 773136
- Draine B. T. et al., 2007, *ApJ*, 663, 866
- Drissen L., Roy J.-R., Moffat A. F. J., Shara M. M., 1999, *AJ*, 117, 1249
- Dunne L., Eales S. A., 2001, *MNRAS*, 327, 697
- Dunne L., Eales S., Edmunds M., Ivison R., Alexander P., Clements D. L., 2000, *MNRAS*, 315, 115
- Elmegreen D. M., Elmegreen B. G., 1982, 201, 1021
- Elmegreen D. M., Elmegreen B. G., 1987, 314, 3
- Engelbracht C. W., Gordon K. D., Rieke G. H., Werner M. W., Dale D. A., Latter W. B., 2005, *ApJ*, 628, L29
- Engelbracht C. W. et al., 2010, *A&A*, 518, L56
- Flagey N., Boulanger F., Verstraete L., Miville Deschênes M. A., Noriego Cespo A., Reach W. T., 2006, *A&A*, 453, 969
- Freedman W. L. et al., 2001, *ApJ*, 553, 47
- Galametz M. et al., 2010, *A&A*, 518, L55
- Garnett D. R., Shields G. A., 1987, *ApJ*, 317, 82
- Gordon K. D. et al., 2005, *PASP*, 117, 50
- Gordon K. D. et al., 2007, *PASP*, 119, 1019
- Gordon K. D., Engelbracht C. W., Rieke G. H., Misselt K. A., Smith J.-D. T., Kennicutt R. C. Jr., 2008, *ApJ*, 682, 336
- Griffin M. J. et al., 2009, in Oschmann J. M. Jr. de Graauw M. W. M., MacEwen H. A., eds, *Proceedings of the SPIE, Space Telescopes and Instrumentation 2008: Optical, Infrared, and Millimeter*. SPIE, Bellingham, p. 70102
- Griffin M. J. et al., 2010, *A&A*, 518, L3
- Herschel Space Observatory, 2010a, *PACS Observer's Manual*, Version 2.1, ESA, Noordwijk
- Herschel Space Observatory, 2010b, *SPIRE Observer's Manual*, Version 2.2, ESA, Noordwijk
- Hinz J. L. et al., 2004, *ApJS*, 154, 259
- Hodge P. W., Kennicutt R. C. Jr., 1983, *AJ*, 88, 296
- Jarrett T. H., Chester T., Cutri R., Schneider S. E., Huchra J. P., 2003, *AJ*, 125, 525
- Karachentsev I. D. et al., 2002, *A&A*, 383, 125
- Kennicutt R. C. Jr., 1998a, *ARA&A*, 36, 189
- Kennicutt R. C. Jr., 1998b, *ApJ*, 498, 541
- Kennicutt R. C. Jr. et al., 2003, *PASP*, 115, 928
- Kennicutt R. C. Jr. et al., 2007, *ApJ*, 671, 333
- Kennicutt R. C. Jr. et al., 2009, *ApJ*, 703, 1672
- Kessler M.F. et al. 1996, *A&A*, 315, L27
- Kong X., Charlot S., Brinchmann J., Fall S. M., 2004, *MNRAS*, 349, 769
- Li A., Draine B., 2001, *ApJ*, 554, 778
- Lonsdale Persson C. J., Helou G., 1987, *ApJ*, 314, 513
- Lutz D., 2010, *PACS photometer point spread function*, Version 1.01, ESA, Noordwijk

- Markoff S. et al., 2008, *ApJ*, 681, 905
- Mentuch E. et al., 2009, *ApJ*, 706, 1020
- Mentuch E., Abraham R. G., Zibetti S., 2010, *ApJ*, 725, 1971
- Meurer G. R., Heckman T. M., Calzetti D., 1999, *ApJ*, 521, 64
- Meurer G. R. et al., 2006, *ApJS*, 165, 307
- Moustakas J., Kennicutt R. C. Jr., Tremonti C. A., Dale D. A., Smith J.-D. T., Calzetti D., 2010, *ApJS*, 190, 233
- Neugebauer G. et al., 1984, *ApJ*, 278, L1
- Ott S., 2010, in Mizumoto Y., ed., *ASP Conf. Ser. Vol. 434, Astronomical Data Analysis Software and Systems XIX*. Astron. Soc. Pac., San Francisco, p. 139
- Pilbratt G. et al., 2010, *A&A*, 518, L1
- Poglitsch A. et al., 2010, *A&A*, 518, L2
- Popescu C. C., Tuffs R. J., Dopita M. A., Fischera J., Kylafis N. D., Madore B. F., 2011, *A&A*, 527, A109
- Prescott M. K. M. et al., 2007, *ApJ*, 668, 182
- Rieke G. H. et al., 2004, *ApJS*, 154, 25
- Rowan-Robinson M. et al., 2010, *MNRAS*, 409, 2
- Sauvage M., Thuan T. X., 1992, *ApJ*, 396, L69
- Schlegel D. J., Finkbeiner D. P., Davis M., 1998, *ApJ*, 500, 525
- Schmidt M., 1959, *ApJ*, 129, 243
- Scoville N., Young J. S., 1983, *ApJ*, 265, 148
- Smith B. J., Hancock M., 2009, *AJ*, 138, 130
- Stansberry J. A. et al., 2007, *PASP*, 119, 1038
- Talbot R. J. Jr., Jensen E. B., Dufour R. J., 1979, *ApJ*, 229, 91
- Telesco C. M., Harper D. A., 1980, *ApJ*, 235, 392
- Thim F., Tammann G. A., Dolphin A., Sandage A., Tolstoy E., Labhardt L., 2003, *ApJ*, 590, 256
- Trinchieri G., Fabbiano G., Palumbo G. G. C., 1985, *ApJ*, 290, 96
- Turner J. L., Ho P. T. P., Beck S. C., 1987, *Ap*, 313, 644
- Verley S. et al., 2010, *A&A*, 518, L68
- Véron P., Sauvayre A., 1965, *AnAp*, 28, 698
- Walterbos R. A. M., Greenawalt B., 1996, *ApJ*, 460, 696
- Walterbos R. A. M., Schwering P. B. W., 1987, *A&A*, 180, 27
- Werner M. W. et al., 2004, *ApJS*, 154, 1
- Xilouris E. M., Byun Y. I., Kylafis N. D., Paleologou E. V., Papatourakis J., 1999, *A&A*, 344, 868
- Young L. M., Bendo G. J., Lucero D., 2009, *AJ*, 137, 3053
- Zhu Y.-N., Wu H., Cao C., Li H.-N., 2008, *ApJ*, 686, 155